J. Fluid Mech. (2022), *vol*. 947, A23, doi:10.1017/jfm.2022.646

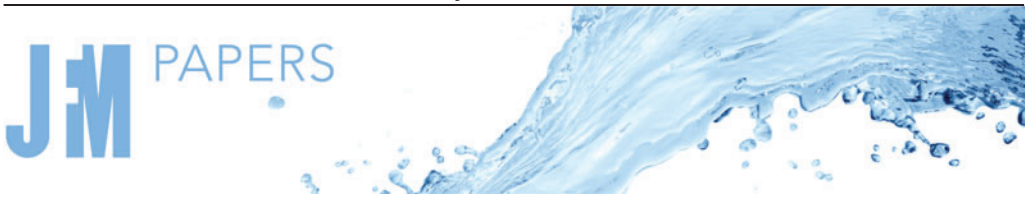

Perforation effects on the wake dynamics of normal flat plates

Abhinav Singh[1] **and Vagesh D. Narasimhamurthy**[1],†

[1]Department of Applied Mechanics, Indian Institute of Technology Madras, Chennai 600036, India

(Received 9 October 2021; revised 15 July 2022; accepted 19 July 2022)

The effect of perforation on the wake of a thin flat plate placed normal to the free stream at Reynolds number (*Re*) 250 (based on plate width d, and inflow velocity U_o) is studied by means of direct numerical simulation. The perforated plate of length $6d$ consist of six equidistant square holes of varying sizes corresponding to porosity β (ratio of open area to total plate area) of 0 %, 4 %, 9 %, 12.25 %, 16 %, 20.25 % and 25 %. It is observed that the bleed or jet flow through perforations pushes the shear layer interaction farther downstream with increasing β. This causes a monotonic decrease in the drag coefficient with increasing porosity, and a sharp fall seeming to begin at $\beta \approx 4\,\%$. On the other hand, the Strouhal number increases with β up to 16 % (at $\beta = 16\,\%$, loss of flow three-dimensionality leads to a 'quasi-laminar' state of flow). This is followed by a sharp fall in the Strouhal number at $\beta \approx 20\,\%$. The behaviour of the large-scale vortical structures in the far wake is influenced by the near-wake behaviour of the bleed flow, where the local *Re* based on the perforation hole size determines the overall flow three-dimensionality. It is also observed that the jet or bleed flow undergoes meandering instability when pitch separation is equivalent to the hole size (at $\beta = 25\,\%$). The low-*Re* turbulent flow for a non-perforated plate is altered to a transitional state by the presence of perforation. The streamwise vortex pairs (secondary instabilities) become fairly organized as β is increased from 0 % to 16 %. The secondary instability at $\beta = 16\,\%$ appears similar to mode-B with wavelength $\approx 1d$. On the contrary, the secondary instability at $\beta = 25\,\%$ appears similar to mode-A with a wavelength of $\approx 2d$.

Key words: turbulence simulation, wakes, vortex streets

† Email address for correspondence: vagesh@iitm.ac.in

1. Introduction

Bluff-bodies are often porous or perforated in applied scenarios. Perforated bodies find application in the process of aggregation, sedimentation and filtration (e.g. design of industrial gauzes and flue exhaust systems). They are also utilized in electronic cooling systems, multi-jet burners, grated decks and fences (Kim & Lee 2002). In addition, Sha & Launder (1979) modelled pipe bundles as porous bluff-body wakes. More recently, perforated bodies have been used to model wind turbine wake phenomena (Xiao *et al.* 2013; Steiros & Hultmark 2018).

The earliest work in this subject was carried out by Taylor (1944), who studied the wake from perforated flat plates. Following Taylor (1944), some attempts have been made to investigate this problem. However, the most comprehensive study has been reported by Castro (1971). In his study, flow past perforated flat plates is classified into two regimes based on the porosity β (ratio of the open area to the total plate area). In the low porosity regime, $\beta < 20\,\%$, the 'near' wake was characterized by a dominant Kármán vortex street, which ceased to exist for higher β (Castro 1971). This regime change seems to be quite sudden at $\beta \approx 20\,\%$. Castro (1971) further reported abrupt changes in the measurements of drag coefficient C_D, Strouhal number St and peak streamwise turbulence intensity u_{rms}/U_∞ around this critical β. The limited literature available in this area further indicates that porosity alone is the dominant geometrical parameter characterizing this flow (Castro 1971; Huang *et al.* 1995; Huang & Keffer 1996; Huang, Kawall & Keffer 1996). In the study of flow over a perforated fence with different hole shapes, Perera (1981) found that the wake structure far downstream of the fence was affected mainly by the porosity, and was independent of the hole shape. In a recent study by Bae & Kim (2016), for a steady laminar wake they found drag coefficient dependence on both porosity and hole shape. It is therefore not clear why this regime shift occurs around 20 % porosity, and why porosity alone dominates the wake phenomenon.

The prior studies in this area further disagree with the reasons for strong periodicity in the 'far' wake of perforated bluff bodies of higher β ($>20\,\%$). Some suggest that the growth of large-scale unsteady structures in the 'far' wake is due to hydrodynamic instability of the mean flow in the absence of a vortex street (Castro 1971; Cimbala, Nagib & Roshko 1988). It is suggested that the two shear layers separated by the bleed flow coalesce some way downstream such that the wake becomes unstable and begins to 'flap'. Here, it is said that there is just enough 'bleed' flow to prevent the formation of a vortex street. Others propose that the small-scale vortices in the formation region (i.e. near the body) merge to form quasi-periodic Kármán-like structures (Huang *et al.* 1995; Huang & Keffer 1996). The study by Wygnanski, Champagne & Marasli (1986) also reported the phenomenon, but the reason for strong unsteadiness in their porous bluff-body wake is not apparent.

The critical transition Reynolds number Re_c for a non-perforated flat plate placed normal to the free stream is ≈105–110. According to Julien, Lasheras & Chomaz (2003), Julien, Ortiz & Chomaz (2004) and Thompson *et al.* (2006), the route-to-transition in the wake of non-perforated flat plates takes place in two stages: first through a quasi-periodic mode of wavelength $\lambda = 5d$–$6d$ at $Re_c \approx 105$–110; and thereafter through mode A of wavelength $\lambda \approx 2d$ at $Re_c \approx 125$. Quasi-periodicity is the property of a system that displays irregular periodicity. In comparison, the circular cylinder wake becomes unstable to mode A at $Re \approx 190$, followed by bifurcation to mode B at $Re \approx 230$–240 (Williamson 1988). Here, mode A is characterized by an antisymmetric pattern of streamwise vortices from one braid region to the next, with wavelength ≈$4D$, where D is the cylinder diameter; and

Reference	Re	Regime	β (%)	Geometry	Method
Castro (1971)	25 000–90 000	Turbulent	0–64.5	Plate	Expt
Graham (1976)	10^4	Turbulent	23–62	Plate	Expt
Liu, Ting & Rankin (2004)	15 000–29 000[a]	Turbulent	40–65	Plate	Expt
Steiros & Hultmark (2018)	6000	Turbulent	10–60	Plate	Expt
Bae & Kim (2016)	25[a]	Laminar	10–40	Plate	Sim
Perera (1981)	—	Turbulent	0–50	Fence	Expt
Kim & Lee (2002)	2985	Turbulent	38.5	Fence	Expt
Alfonsi, Primavera & Felisari (2003)	13 300[a]	Turbulent	—	Hexagon	LES
Cimbala *et al.* (1988)	3000–9000	Turbulent	53	Mesh	Expt
Villermaux & Hopfinger (1994)	$O[10^2]$–$O[10^3]$[a]	Turbulent	8–13	Mesh	Expt
Wygnanski *et al.* (1986)	2000	Turbulent	30–70	Mesh	Expt
Huang *et al.* (1996)	11 000	Turbulent	40	Mesh	Expt
Kopp & Keffer (1996)	5000	Turbulent	30	Mesh	Expt
Antonia, Zhou & Romano (2002)	204[b]	Turbulent	46	Mesh	Expt
Inoue (1985)	$O[10^3]$	Turbulent	25–75	Mesh	DVM
Liu *et al.* (2017)	10 000	Turbulent	12	Disk	Expt
Xiao *et al.* (2013)	32 000	Turbulent	25	Disk	Expt
Cannon, Champagne & Glezer (1993)	13 200	Turbulent	15–50	Disk	Expt
Bevilaqua & Lykoudis (1978)	10^4	Turbulent	82	Disk	Expt
Higuchi *et al.* (1998)	7400	Turbulent	15.8–43.4	Disk	Expt
Kang *et al.* (1989)	10^4–10^5	Turbulent	—	Disk	RANS

Table 1. Flow over various perforated bodies. Here, superscripts [a] and [b] refer to Re based on hole and Taylor-microscale, respectively; Expt means experiment; Sim means simulation; DVM means discrete vortex method; LES means large-eddy simulation; RANS means Reynolds-averaged Navier–Stokes).

mode B is defined as a secondary vortex structure with a symmetric pattern of streamwise vortices with wavelength $\approx 1D$. At this stage, it is not clear how a transitional wake or a wake that is barely turbulent or experiencing transition-to-turbulence would respond to perforation (cf. table 1). The presence of perforation can further complicate the transition process since the jet of fluid emanating through the holes in the base region may affect the growth of secondary instabilities favourably or adversely.

Further, the characteristics of the jet or the 'bleed' flow through the holes itself has received modest attention. Kim & Lee (2001, 2002) in their experimental study of flow over a fence observed that for a given β, hole size affects the upstream flow retardation and jet coalescence downstream of the body. The upstream flow retardation has been found to increase with reduction in hole size, while the jet coalescence and mixing increased with increase in hole dimension. This is reasonable since one can expect the jets to behave in an isolated fashion when the pitch separation c between them is sufficiently large compared to the hole dimension h). On the contrary, if the pitch c/h or the gap is sufficiently small, then the adjacent shear layers can experience proximity interference effects leading to engulfment or meandering oscillations and instabilities (Dadmarzi *et al.* 2018). Villermaux & Hopfinger (1994) have reported a low-frequency (longitudinal) oscillation of the jet merging distance in their experimental study of co-flowing jets from a perforated body. To our knowledge, no other studies have explored this jet or 'bleed' flow characteristic and its immediate effect on the 'near'-wake vortex dynamics of a perforated plate. Note that in addition to the co-flowing or neighbouring jets interaction, complex interference occurs also between the jets and the wake (shear layers emanating from the two edges of the plate), thus leading to jet–wake coupling.

Table 1 summarizes the literature concerning various studies of perforated bodies. Note that most of the perforated geometries were considered in an internal flow configuration. Barring Bae & Kim (2016), all the other studies have investigated high-Reynolds-number flows in the turbulent regime, and none exists on the 'transitional' or low-Reynolds-number turbulent regime. In addition, the problem has (unfortunately) received little attention from the numerical community (especially the direct and large-eddy simulation community). This, along with the concerns raised in the previous paragraphs, clearly demands a detailed investigation. We therefore aim to explore some of those mechanisms and the intricate flow physics through a direct numerical simulation (DNS) study; DNS as a scientific tool is the natural choice to probe such a complex wake phenomenon, since it enables complete access to the instantaneous three-dimensional data. With the aid of vortical structures, spectral analysis, spatio-temporal maps, and single- and multi-point statistics, we wish to disseminate answers to some of the open questions and also report new observations.

2. Problem definition and numerical details

In the current DNS study, the Reynolds number is set to $Re_d = U_o d/\nu = 250$, where U_o and d refer to inflow velocity and plate width, respectively. This Reynolds number corresponds to the DNS study of a non-perforated flat plate wake by Najjar & Balachandar (1998). Note that this $Re_d = 250$ is well above the critical transition Reynolds number ($\approx$105–110) for a non-perforated flat plate placed normal to the free stream.

The present set-up is shown in figure 1. Unless stated explicitly, all spatial dimensions are scaled by d, and all velocity fields are normalized by U_o. Figure 1(b) shows the perforation pattern, where a plate of width d, thickness $0.02d$ and length $L_y = 6d$ is considered with six equidistantly spaced square holes arranged in an in-line fashion. Here, c and m refer to the pitch separation and the mid-gap between the holes, respectively. The porosity β is determined through the hole dimension h and number of holes n, i.e. $\beta = (nh^2/L_y d) \times 100\,\%$. In the present study, $\beta = 0\,\%, 4\,\%, 9\,\%, 12.25\,\%, 16\,\%, 20.25\,\%$ and $25\,\%$ are considered (i.e. corresponding to $h/d = 0$, 0.2, 0.3, 0.35, 0.4, 0.45 and 0.5, respectively). Note that the present plate thickness, $0.02d$, is same as that used in other numerical studies and is classified as 'thin' in the literature (Narasimhamurthy, Andersson & Pettersen 2008; Narasimhamurthy & Andersson 2009; Afgan *et al.* 2013; Choi & Yang 2014; Tian *et al.* 2014; Hemmati, Wood & Martinuzzi 2016; Dadmarzi *et al.* 2018). The length of the plate, $L_y = 6d$, is chosen based on a domain verification study (see Appendix B and also Singh & Narasimhamurthy 2018, 2021), where L_y is varied from $1d$ to $12d$.

Figure 1 shows the three-dimensional (3-D) computational domain, where L_x, L_z and L_y denote streamwise, cross-stream and spanwise lengths, respectively. The plate is positioned at $5d$ downstream of the inflow. This domain is nearly the same as that used in other DNS studies of wake from non-perforated plates (cf. table 2 and Appendix B and C). The current mesh ($320 \times 240 \times 260$), however, is more refined than others, especially in the cross-stream (N_z) and spanwise (N_y) directions owing to the perforation pattern. The grid resolution around the plate is set as $[\Delta_x, \Delta_y, \Delta_z] = [0.01, 0.025, 0.025]$. This numerical mesh is achieved based on a detailed grid verification test (see Appendix A and also Singh & Narasimhamurthy 2021).

The incompressible Navier–Stokes equations are solved in 3-D space and time using the parallel finite volume code MGLET (Manhart 2004) with staggered Cartesian mesh. The spatial terms of the governing equations are discretized using a second-order central difference scheme, while the numerical solution is marched forward in time

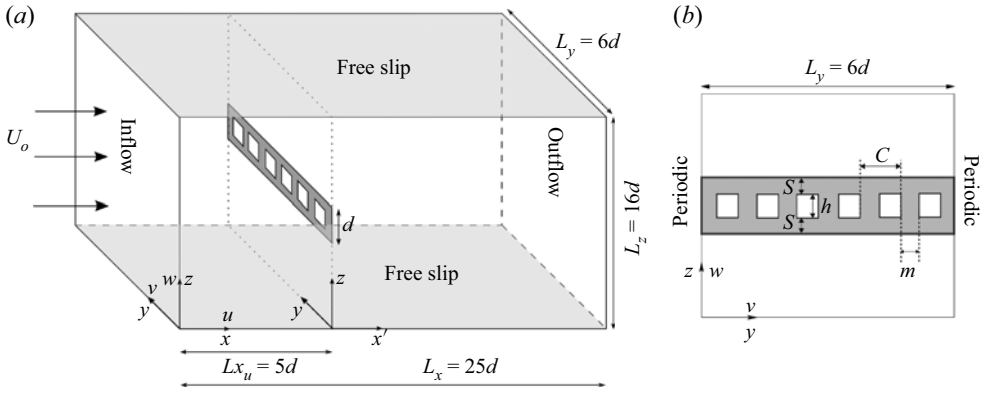

Figure 1. (*a*) Three-dimensional computational domain (not to scale). Here, x is the global streamwise coordinate, while x' denotes the local streamwise coordinate with its origin at the plate location. (*b*) Side view depicting the perforated plate details.

using a third-order explicit Runge–Kutta scheme. The Poisson equation is solved using the iterative strongly implicit procedure (SIP) method. A uniform velocity profile U_o (without any free stream perturbations) and a Neumann boundary condition for the pressure are prescribed as inflow. A free-slip condition is used on both top and bottom boundaries, while a periodic boundary condition is applied for the side boundaries (cf. figure 1). For outflow, a Neumann boundary condition is used for velocities and the pressure is set to zero. A direct forcing immersed boundary method (Peller *et al.* 2006; Narasimhamurthy *et al.* 2008) is used for converting the no-slip and impermeability boundary conditions on the plate into internal boundary conditions of the computational grid using a third-order-accurate least-squares interpolation scheme. A recent DNS study of wakes by Dadmarzi *et al.* (2018) observed that initial conditions can alter significantly the final converged solution and thereby recreate many distinct states of flow reported independently in the literature. In the current study, therefore, all the simulations are started with the same initial conditions (a quiescent state). The time step is chosen as $\Delta t = 0.001d/U_o$, and the number of Poisson iterations per time step is set to a maximum value of 60 (to achieve numerical residue 10^{-6}). Parallelization is executed through a message passing interface (MPI). The simulations are run on an IBM System x iDataPlex dx360 M4 and a Dell PowerEdge R740 parallel computers. The wall clock times for $\beta = 0\,\%$, $4\,\%$, $9\,\%$, $12.25\,\%$, $16\,\%$, $20.25\,\%$ and $25\,\%$ are about 251, 827, 938, 718, 1397, 635 and 1137 h, respectively, with associated CPU times of about 16 046, 32 833, 60 038, 35 388, 89 433, 31 224, 72 757 h, respectively.

2.1. *Flow past a non-perforated plate*

As a reference case, flow over a non-perforated flat plate placed normal to the free stream is simulated, and the results are compared with the simulations of Najjar & Balachandar (1998). Both two-dimensional (2-D) and three-dimensional (3-D) simulations are performed as the reference case (Najjar & Balachandar 1998). Figure 2 shows very good agreement of the mean pressure coefficient between the 2-D and 3-D cases, respectively. Here, the mean pressure coefficients on the front and back of the plate are defined as $\bar{C}_{p,front} = (\bar{p}_{front} - \bar{p}_{inlet})/(0.5\rho U_o^2)$ and $\bar{C}_{p,back} = (\bar{p}_{back} - \bar{p}_{inlet})/(0.5\rho U_o^2)$, respectively, where p is the pressure. Further, the mean drag coefficient $\overline{C_d} =$

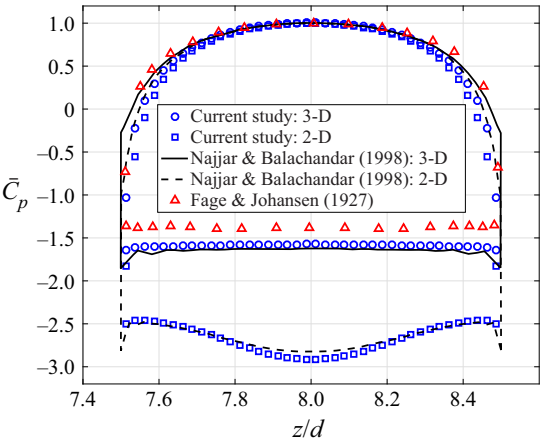

Figure 2. Mean pressure coefficient over a non-perforated plate at $Re_d = 250$. Experimental data of Fage & Johansen (1927) are at $Re_d = 1.5 \times 10^5$. The top and bottom halves of the curve signify the data from the front and back of the plate, respectively.

Reference	Re_d	$N_x \times N_y \times N_z$	L_{x_u}	L_{x_d}	L_z	L_y
Hemmati *et al.* (2016)	1200	$256 \times 64 \times 202$	$5d$	$20d$	$16d$	$2\pi d$
Najjar & Vanka (1995)	1000	$256 \times 32 \times 256$	$8d$	$20d$	$16d$	$2\pi d$
Narasimhamurthy & Andersson (2009)	750	$512 \times 60 \times 384$	$5d$	$20d$	$16d$	$6d$
Najjar & Balachandar (1998)	250	$192 \times 48 \times 128$	$5d$	$20d$	$16d$	$6d$
Current study (perforated plate)	250	$320 \times 240 \times 260$	$5d$	$20d$	$16d$	$6d$

Table 2. Numerical mesh and domain details in various DNS studies of flow over normal flat plates. Here, L_{x_u} and L_{x_d} refer to the upstream and downstream extents of the domain from the plate location, respectively, while L_y and L_z correspond to the spanwise and cross-stream lengths, respectively.

Simulation type	Reference	Re_d	$\overline{C_d}$	St_d
3-D	Najjar & Balachandar (1998)	250	2.36	0.16
2-D	Najjar & Balachandar (1998)	250	3.36	0.139
3-D	Current study	250	2.22	0.164
2-D	Current study	250	3.29	0.152

Table 3. Results from non-perforated plate simulations.

$(\bar{p}_{front} - \bar{p}_{back})/(0.5\rho U_o^2)$, and the Strouhal number $St_d = fd/U_o$, as given in table 3, show very good agreement between the simulations. Here, f is the dominant frequency in the wake.

3. Results and discussions

In the present study, the instantaneous quantity $\phi \in (u, v, w, p)$, recorded at a statistically stationary state, is decomposed into the time mean component $\bar{\phi}$ and the fluctuations $\hat{\phi}$. Here, $\hat{\phi}$ comprises both coherent and random motion.

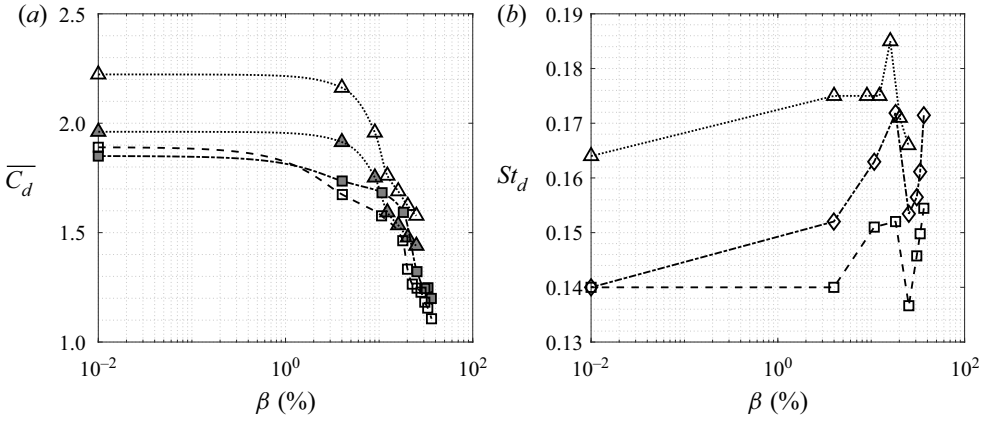

Figure 3. Comparison of the mean quantities obtained in the current DNS with the experiments of Castro (1971). (*a*) Drag coefficient $\overline{C_d}$: open triangle denotes current DNS at $Re_d = 250$ ($\overline{C_d} = 2.223$ at $\beta = 0\,\%$); grey triangle denotes blockage corrected DNS at $Re_d = 250$ ($\overline{C_{d_c}} = 1.961$ at $\beta = 0\,\%$); grey square denotes wake traverse method at $Re_d = 9 \times 10^4$ ($\overline{C_d} = 1.85$ at $\beta = 0\,\%$); open square denotes drag balance method at $Re_d = 9 \times 10^4$ ($\overline{C_d} = 1.89$ at $\beta = 0\,\%$) (Castro 1971). (*b*) Strouhal number St_d: open triangle denotes current DNS at $Re_d = 250$ at $15d$ downstream of the plate ($St_d = 0.164$ at $\beta = 0\,\%$); open diamond denotes $Re_d = 2.5 \times 10^4$; open square denotes $Re_d = 9 \times 10^4$ ($St_d = 0.14$ at $\beta = 0\,\%$) (Castro 1971). Note that the lines are used to represent the trend.

3.1. *Drag coefficient and Strouhal number*

Figure 3 shows the dependence of the computed drag coefficient $\overline{C_d}$, the blockage-corrected drag coefficient $\overline{C_{d_c}}$, and St_d on β (also reported in table 4). Here, the correction for the drag coefficient due to domain blockage was done using the method of Maskell (1965) (see Appendix C for details). It is readily observed that there is excellent qualitative agreement with the experiments of Castro (1971) despite the large difference in Re between the studies. Figure 3(*a*) shows the monotonic decrease in $\overline{C_d}$ with increasing β. However, its sharp fall is observed to be occurring much earlier than the $\beta \approx 20\,\%$ reported by Castro (1971). In the current DNS, an apparent reduction in drag is observed to start at $\beta \approx 4\,\%$. The exact location of the sudden drop cannot be determined due to a limited number of data points. Such a phenomenon arises because the vortex street formation region, where the separated shear layers begin to interact, is pushed further downstream as a result of the bleed flow through the plate (explained further in § 3.2). On the other hand, figure 3(*b*) shows that the increase in St_d with respect to β followed by a sudden drop at $\beta \approx 20\,\%$ is well predicted by the current DNS. Here, the blockage effect could have an influence on St_d values reported in both studies. Note that the blockage ratio is almost the same in both studies. Additionally, the present DNS shows a higher St_d as opposed to the experiments of Castro (1971). Such an increase in St_d is attributed to a reduction in Re_d. Nevertheless, contrary to the observations of Castro (1971), it is quite interesting to observe that the sudden drop in $\overline{C_d}$ occurs at different β in the present DNS, which could be an effect of the large difference in Re. Therefore, figure 3 demands further investigation to determine the mechanism for such a behaviour. Since the wake dynamics is believed to be following the general trend at intermediate porosities, and also for brevity, only $\beta = 0\,\%$, $9\,\%$, $16\,\%$ and $25\,\%$ have been discussed in detail in the following sections.

Parameter	$\beta = 0\,\%$	$\beta = 4\,\%$	$\beta = 9\,\%$	$\beta = 12.25\,\%$	$\beta = 16\,\%$	$\beta = 20.25\,\%$	$\beta = 25\,\%$
$St_{d,x'/d\geqslant 5}$	0.164	0.175	0.175	0.175	0.185	0.171	0.166
$St_{d,x'/d=1}$	0.164	0.175	0.175	0.24	—	—	$O[10^{-2}]$
$\overline{C_d}$	2.223	2.162	1.958	1.761	1.689	1.622	1.577
$\overline{C_{d_c}}$	1.961	1.914	1.752	1.593	1.534	1.478	1.440
$\bar{u}/U_{ojet,max}$	—	—	1.4889	—	1.4017	—	1.3663
E_{peak}	440	—	4324	—	12 662	—	3964
b_z/d	2.3635	—	1.1538	—	0.9232	—	1.2781
b_x/b_z	1.0112	—	2.7063	—	2.7178	—	1.8926
v_{rms}	0.1203	—	0.0861	—	0.0409	—	0.0518
w_{rms}	0.1835	—	0.2713	—	0.3741	—	0.2638

Table 4. Mean quantities. The peak spectral energy of the w' velocity (E_{peak}), v_{rms} and w_{rms} are all calculated in the 'far' wake at $15d$ downstream along the top edge of the plate ($y/d = 0$, $z/d = 8.5$). All spectral data are taken for 60 shedding cycles. Since the wake characteristics are believed to be following the general trend at intermediate porosities, only $\beta = 0\,\%$, $9\,\%$, $16\,\%$ and $25\,\%$ have been analysed in detail.

3.2. *Behaviour of the vortex street*

Figures 4(*a*,*c*,*e*,*g*) and 4(*b*,*d*,*f*,*h*) show instantaneous spanwise vorticity contours in side and bottom view, respectively. It appears that perforation induces the shear layers emanating from either side of the plate to interact farther downstream, thereby creating a larger formation region when compared to non-perforated plates. This demarcates the 'near' wake region from the 'far' wake region, where the 'near' wake is characterized by the 'bleeding' jet flow through the holes, and the 'far' wake is characterized by the unsteady vortical structures. It can be inferred that the delayed interaction of the shear layers with increasing β causes the monotonic decrease in $\overline{C_d}$, as shown in figure 3(*a*). Further, a strong 'bleed' flow at $\beta = 16\,\%$ suppresses the vortex shedding at the plate, rendering the vortex-dominated flow quasi-periodic with reduced flow three-dimensionality. The vortex topology is demonstrated further by the iso-contours of the instantaneous λ_2 criterion in figure 5. Here, λ_2 is defined as the second-largest eigenvalue of the tensor $S_{ij}S_{ij} + \Omega_{ij}\Omega_{ij}$, where S_{ij} and Ω_{ij} are the symmetric and antisymmetric parts of the velocity gradient tensor, respectively (Jeong & Hussain 1995). At higher $\beta = 25\,\%$, it is observed that the spanwise vortex tubes undergo flow instabilities in the form of helical twisting and stretching (not evident at this time instant, but discussed in subsequent sections). Figure 5 is further striking and is indicating clearly that an already 'turbulent' state behind a non-perforated plate is tending towards relaminarization and is pushed further into a transitional state by the presence of perforation at the chosen Re. The instability modes will be discussed in further detail in § 3.6.

Next, the vortex characteristics of the first pair of counter-rotating vortex rollers shown in figures 4(*a*,*c*,*e*,*g*) are studied. At a given spanwise location, the circulation Γ_y and the vortex centre X^c of a vortex with vorticity ω_y are calculated by

$$\Gamma_y = \int\int_D \omega_y \,\mathrm{d}x\,\mathrm{d}z, \tag{3.1}$$

$$X^c = \frac{1}{\Gamma_y}\int\int_D X\omega_y \,\mathrm{d}x\,\mathrm{d}z. \tag{3.2}$$

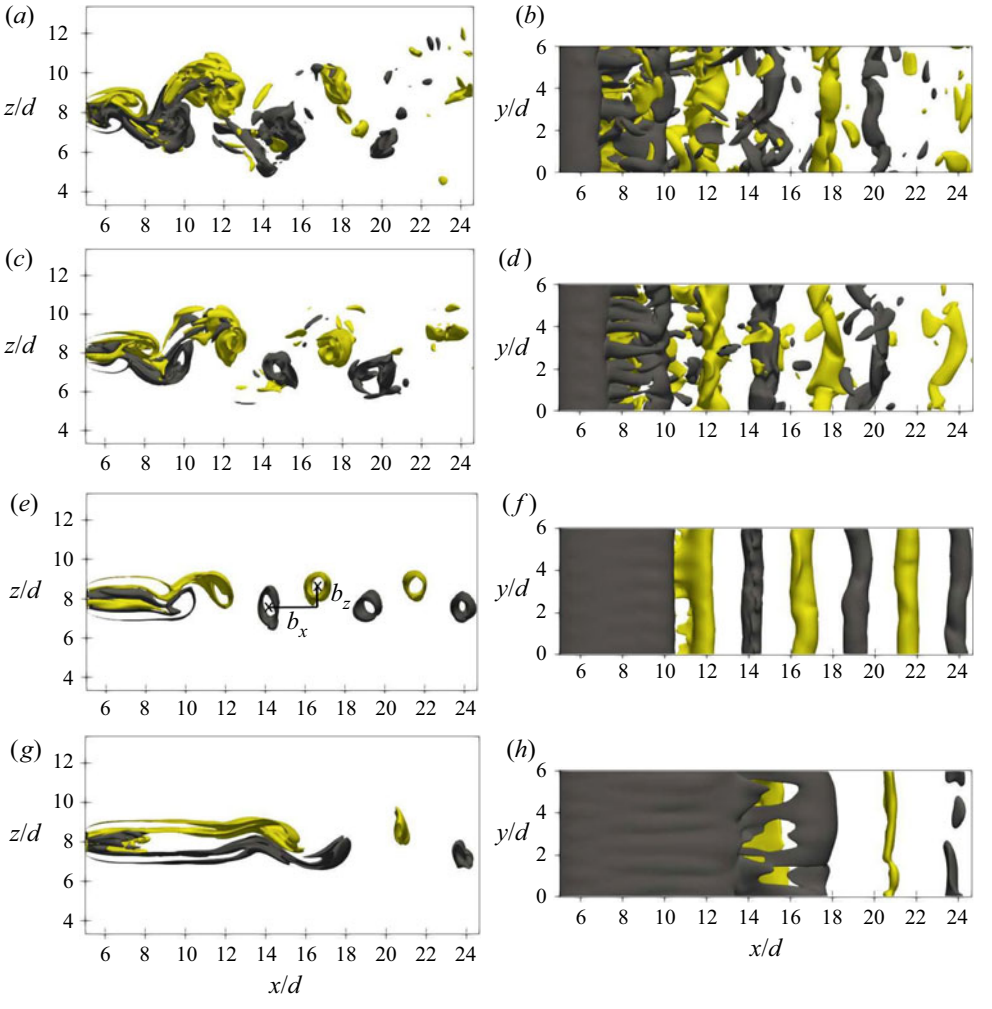

Figure 4. Instantaneous spanwise vorticity $\omega_y = \pm(0.004\text{–}0.005)$: (*a*,*c*,*e*,*g*) side view depicting wake width; (*b*,*d*,*f*,*h*) bottom views, at (*a*,*b*) $\beta = 0\,\%$, (*c*,*d*) $\beta = 9\,\%$, (*e*,*f*) $\beta = 16\,\%$, and (*g*,*h*) $\beta = 25\,\%$.

Here, the domain of integration D signifies the region enclosing the vortex, and X is the coordinate of the surface element $\mathrm{d}x\,\mathrm{d}z$ having vorticity ω_y. The vortex separation distance b between counter-rotating vortices is obtained from

$$b = |X^c_+ - X^c_-|. \tag{3.3}$$

The subscripts '+' and '−' denote the signs of the two counter-rotating vortices. The vortex separation is further decomposed into streamwise component b_x, and cross-stream component b_z.

These vortical quantities are averaged along the span and reported in table 4, where E_{peak} denotes the peak spectral energy associated with the $\hat{w}$ velocity signal, and v_{rms} is used as a sufficient measure of three-dimensionality in the flow (Karniadakis & Triantafyllou 1992). It is observed that the variation of E_{peak} with respect to β follows a trend similar to St_d, where it increases up to $\beta = 16\,\%$ followed by a sharp drop at $\beta = 25\,\%$. In contrast, b_z and

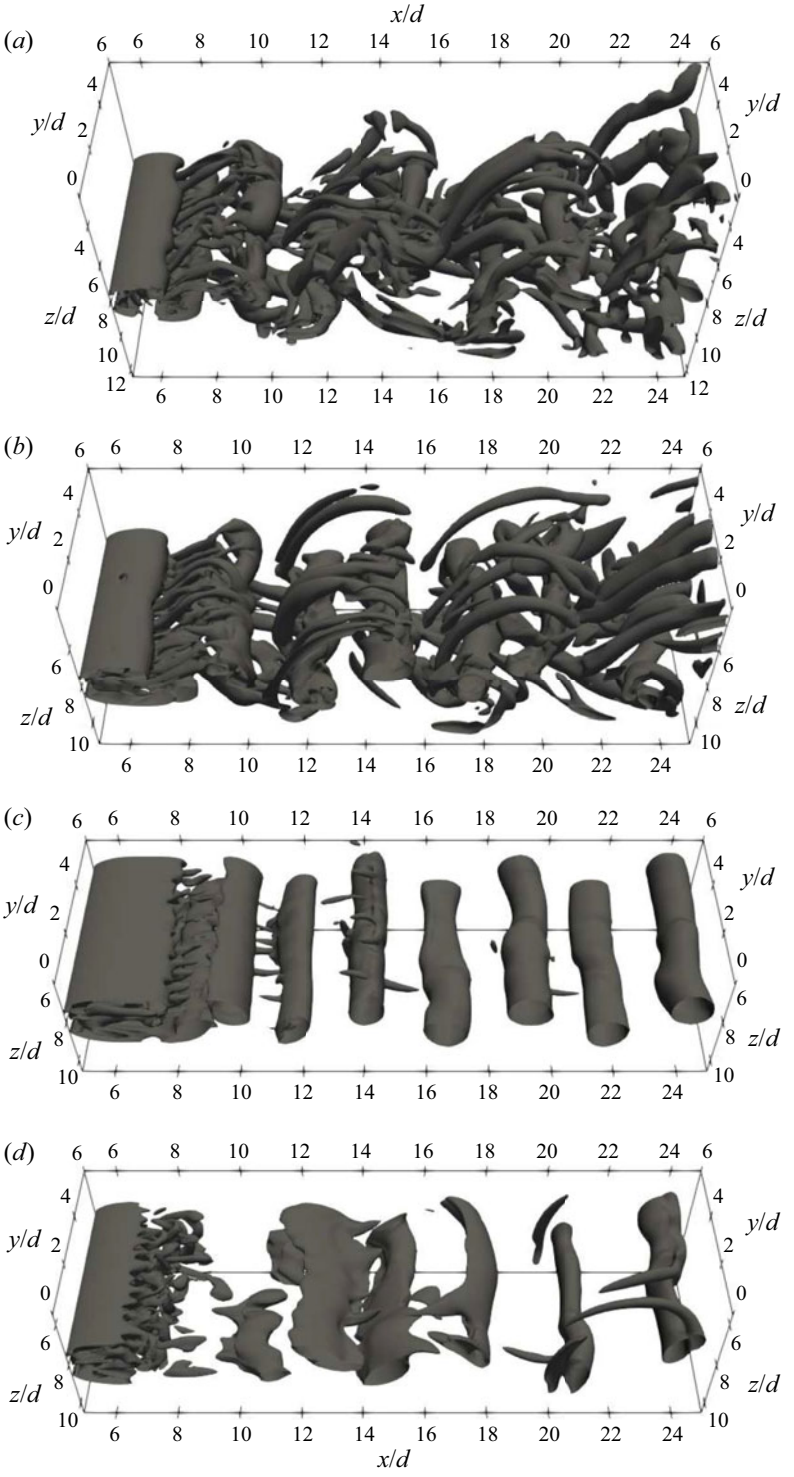

Figure 5. Instantaneous λ_2 from -3×10^{-6} to -4×10^{-6}: (*a*) $\beta = 0\,\%$, (*b*) $\beta = 9\,\%$, (*c*) $\beta = 16\,\%$, (*d*) $\beta = 25\,\%$.

v_{rms} follow an inversely related trend. It can be deduced that as the three-dimensionality in the flow reduces, the counter-rotating vortices are brought closer to each other in the cross-stream direction b_z, causing increased spectral energy E_{peak}. This leads to a larger streamwise separation b_x, with a higher shedding frequency, or St_d.

3.2.1. *Instantaneous fluctuation of kinetic energy*

Figure 6 shows iso-contours of instantaneous fluctuation kinetic energy, defined as $k = \widehat{u_i}\widehat{u_i}/2$. Here, the occurrence of high-intensity spots in the 'near' wake at $\beta > 0\,\%$ corresponds to the length of the 'bleed' jet core. The spanwise coherence of k in the 'far' wake signifies the location of shear layer roll-up. The distribution of fluctuation kinetic energy in the 'near' and 'far' wakes shows clearly that the primary source of fluctuation energy in the 'near' wake is the jets emanating from perforation holes (see figures 6*b*,*d*,*f*,*h*). These jets are separated by wakes from the solid portion of the plate, resulting in an anisotropic and inhomogeneous flow. Such a jet–wake interaction produces a significant amount of shear. It appears that the length of the primary vortex formation around the 'bleed' jet varies with β, similar to the trend followed by St_d. Here, it is observed to increase from $\beta = 9\,\%$ to $\beta = 16\,\%$, followed by a reduction at $\beta = 25\,\%$. At $\beta = 16\,\%$, the length of the 'bleed' jet core nearly coincides with the location of shear layer roll-up, indicating the jet–wake coupling close to equilibrium. On the other hand, the coherent or unsteady motion is responsible for the high-fluctuation kinetic energy in the 'far' wake. Additionally, it could be seen here that the turbulence in the 'near' as well as 'far' wake (also see v_{rms} in table 4) is suppressed gradually as β increases towards 16 % with a corresponding rapid ascent of St_d (see table 4). Because of the changing nature of the small-scale flows through the holes, the turbulence re-emerges at the higher β of 25 %. This is accompanied with a fall in St_d from its elevated values at $\beta = 9\,\%$ and 16 %.

Further, the local Reynolds numbers are shown in table 5. Here, Re_m is defined based on the margin m between two adjacent holes (see figure 1*b*), and Re_h is defined based on the width of the hole, h. The local Reynolds number of the jet, Re_{jet}, is defined as $Re_{jet} = \bar{u}_{jet,max}h/\nu$, where $\bar{u}_{jet}$ indicates the jet centreline velocity, and subscript max signifies maximum value along the centreline. At lower porosities, flow retardation is expected to be high, with vortex street dominating over 'bleed' flow, leading to $Re_{jet} < Re_m$. At higher porosities, 'bleed' flow controls the vortex street due to increased momentum with $Re_{jet} > Re_m$. At $\beta = 16\,\%$, the 'bleed' flow is just enough to prevent the shear layers from interacting in the 'near' wake with $Re_{jet} \approx Re_m$. Thus it could be argued that the peculiar behaviour of quasi-laminar flow with weak three-dimensionality at $\beta = 16\,\%$ is related to the fact that $Re_{jet} \approx Re_m$. Here, the 'bleed' jet is marginally longer with least three-dimensionality, as seen by the relatively lower k in the 'near' wake (see figures 6*b*,*d*,*f*,*h*). At slightly higher $\beta = 25\,\%$, k revives to a larger value, indicating transition of the laminar 'bleed' jet to an irregular state. This could be due to proximity interference effects of adjacent jets when $h \gtrsim m$.

Although the variation of St_d with β in the current DNS follows a trend very similar to high Re cases of Castro (1971), it is quite possible that the wake and 'bleed' flow vortex dynamics might be different at much higher Re. Nevertheless, it was presumed by Castro (1971) that the flow through the holes themselves affects $\overline{C_d}$ and St_d. The observations in this section indicate clearly that the local Reynolds number in the 'near' wake plays a primary role in determining the overall three-dimensionality of the flow, and the 'near' wake affects the behaviour of large vortical structures in the 'far' wake.

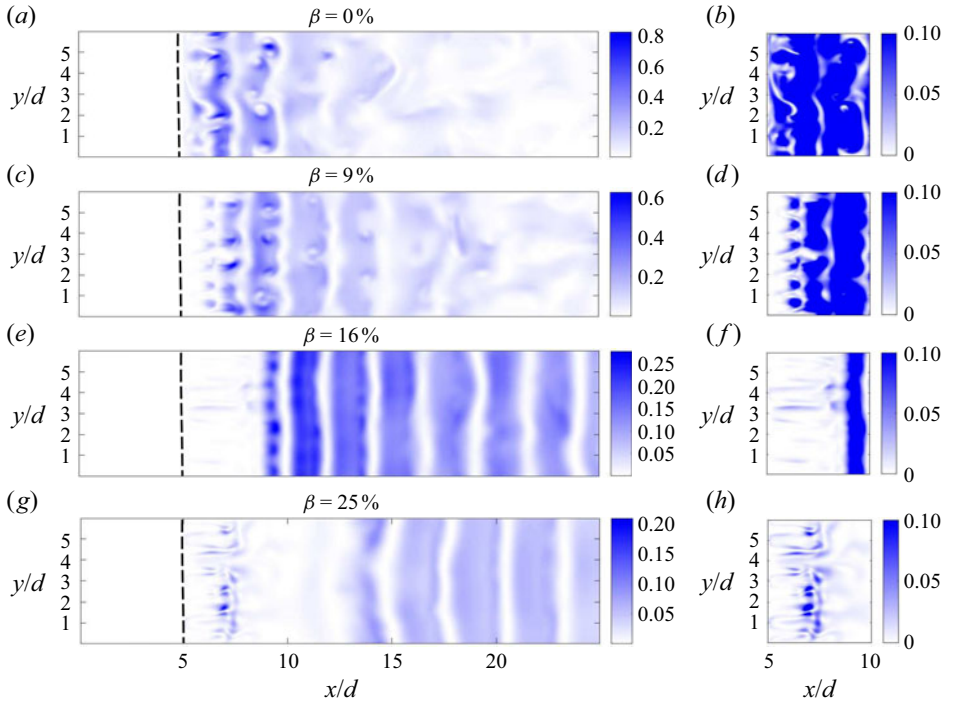

Figure 6. Instantaneous fluctuation kinetic energy at mid z/d plane: (a,c,e,g) whole domain; (b,d,f,h) the 'bleed' jet region ('near' wake). Note that $x/d = 5$ indicates the plate location. Observe that the colour bar ranges differ between panels.

$\beta\%$	Re_h	Re_m	Re_{jet}
0	—	250	—
4	40	200	77
9	75	175	111
12.25	87.5	162.5	124
16	100	150	140
20.25	112.5	137.5	155
25	125	125	170

Table 5. Various Reynolds numbers shown here are defined as $Re_h = U_o h/\nu$, $Re_m = U_o m/\nu$ and $Re_{jet} = \bar{u}_{jet,max} h/\nu$. Here, m is also equal to $2s$ (cf. figure 1b).

3.3. *Spatio-temporal analysis*

Figure 7 shows the spatio-temporal plot of cross-stream velocity w/U_o for various β. Here, the horizontal axis corresponds to the normalized time tU_o/d, and the vertical axis is the spanwise extent of the plate, y/d. The data in figures 7(a,c,e,g) are recorded from the 'near' wake at 1d downstream of the plate, while the data in figures 7(b,d,f,h) stem from the 'far' wake at 15d downstream of the plate. The spanwise alternate bands in the 'far' wake signify a Kármán-like vortex street. It is evident that the coherence in the spanwise bands in the 'far' wake increases with β up to 16 %. In contrast, the incoherence increases from $\beta = 16$ % to 25 %. On the other hand, it is observed that the spanwise vortex structures in

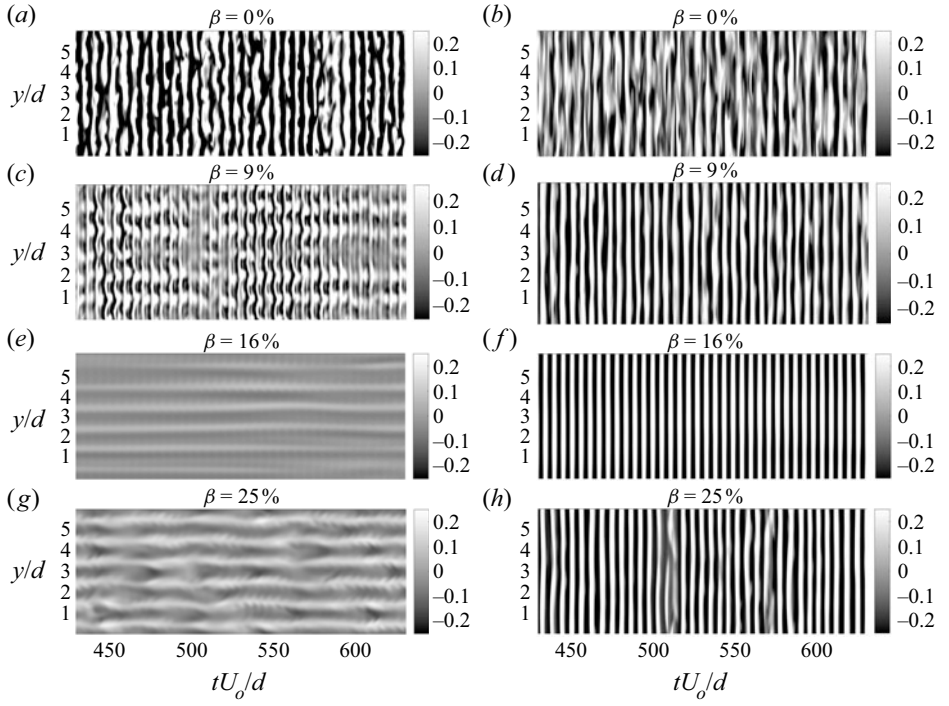

Figure 7. The w velocity time trace sampled in (a,c,e,g) the 'near' wake (1d downstream along the top edge of the plate, $z/d = 8.5$), and (b,d,f,h) the 'far' wake (15d downstream along the top edge of the plate, $z/d = 8.5$).

the 'near' wake transition to streamwise vortex structures with an increase in β. Here, the streamwise alternate bands signify shear layer undulations under the influence of 'bleed' flow. Note that the wavelength of these waves is approximately equal to the geometric pitch of the perforations. Such a flow state in the 'near' wake indicates vortex street suppression at higher β, causing delayed shear layer interaction leading to monotonic decrease in $\overline{C_d}$.

Figures 8 and 9 show the corresponding time trace of the spanwise and cross-stream velocity signals in the 'near' and 'far' wakes, respectively. Figure 8 further supports the vortex street suppression at higher β, demonstrated by reduced irregularities in the v and w velocity signatures. The signals at $\beta = 16\,\%$ are nearly quiescent, indicating vortex street suppression leading to undulating shear layers in the 'near' wake. Here, the quiescent flow also suggests quasi-laminar characteristics. It has already been observed by fluctuation kinetic energy, and it will also be shown later by 'bleed' flow characteristics and secondary instabilities, that a weak three-dimensionality exists at $\beta = 16\,\%$. The revival of three-dimensionality at $\beta = 25\,\%$ could be due to local Re effects where the neighbouring 'bleed' jets interact with each other when $h \gtrsim m$. Further, the 'bleed' jets undergo meandering instability due to proximity interference effects (discussed further in § 3.7). On the other hand, figure 9 demonstrates the vortex street behaviour in the 'far' wake. The w velocity signal at $\beta = 0\,\%$, coupled with higher fluctuations in the v velocity, indicates the irregular behaviour of the vortex street. With increasing β, the irregularities reduce, leading to a quasi-periodic state with weak three-dimensionality at $\beta = 16\,\%$. At $\beta = 25\,\%$, the v velocity fluctuations increase, indicating revival of three-dimensionality in the flow. Overall, it is clear that the low-Re turbulent state at $\beta = 0\,\%$ is pushed back

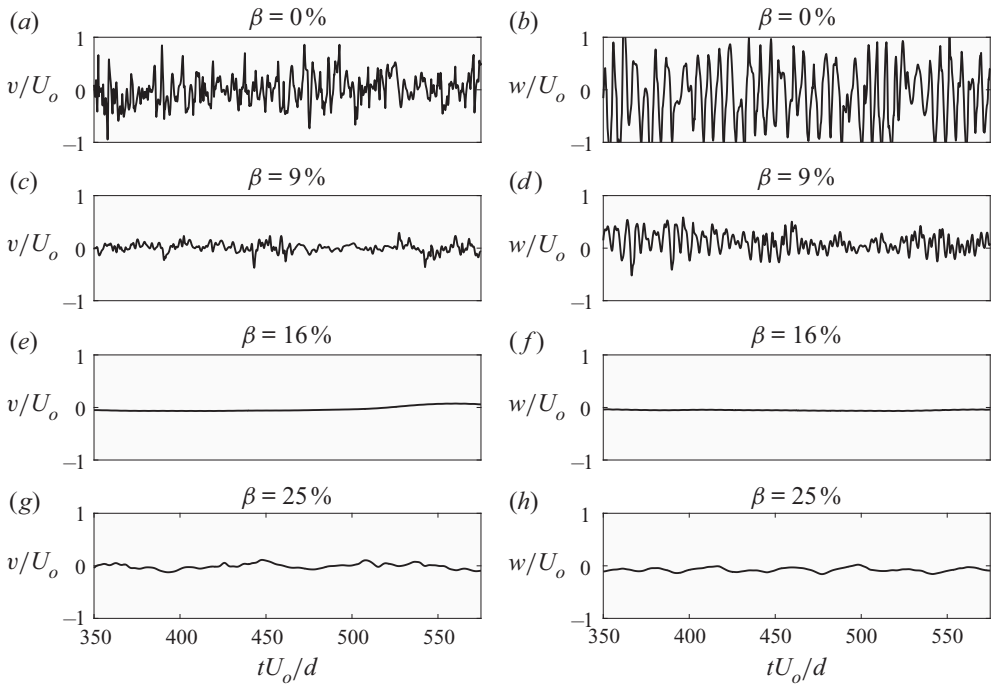

Figure 8. Velocity time trace sampled in the 'near' wake (1d downstream of the plate along the top edge of the plate, $y/d = 0$, $z/d = 8.5$): (a,c,e,g) v/U_o, (b,d,f,h) w/U_o.

to a transitional state by the perforations. A similar phenomenon is also reported in the wakes of circular cylinders, where addition of dilute concentrations of polymer additives causes turbulence suppression (Richter, Iaccarino & Shaqfeh 2010, 2012).

3.4. *Spectral analysis*

Fast Fourier transforms of the instantaneous $\hat{w}$ velocity signal sampled over 60 vortex shedding cycles are shown in figure 10. Figures 10(a,c,e) show the Fourier spectrum of the signal in the 'near' wake, whereas figures 10(b,d,f) show that of the 'far' wake. Here, f_s denotes the Strouhal number corresponding to the dominant frequency. Figures 10(a,b) show that the dominant St_d is the same in both the 'near' and 'far' wakes for $\beta = 9\,\%$, signifying that the effect of the 'bleed' jet is not strong enough to push the formation of a vortex street downstream by a significant margin. In the $\beta = 16\,\%$ case, distinct dominant frequencies emerge. Figures 10(c,d) show that in the 'near' wake spectrum, the most dominant frequency corresponds to $St_d = O[10^{-3}]$, which is insignificant. The next distinct value, $St_d = 0.185$, interestingly becomes the most dominant one in the 'far' wake. Note that a single dominant frequency was reported in Castro (1971), where the origin of the signal recording position is not particularly clear. (Note that Castro (1971) used circular holes and the experiments were conducted at higher Re.) In addition, figures 10(c,d) also show the presence of distinct higher harmonics of the Strouhal frequency containing a specific periodicity, further supporting the quasi-laminar behaviour described in the previous subsections.

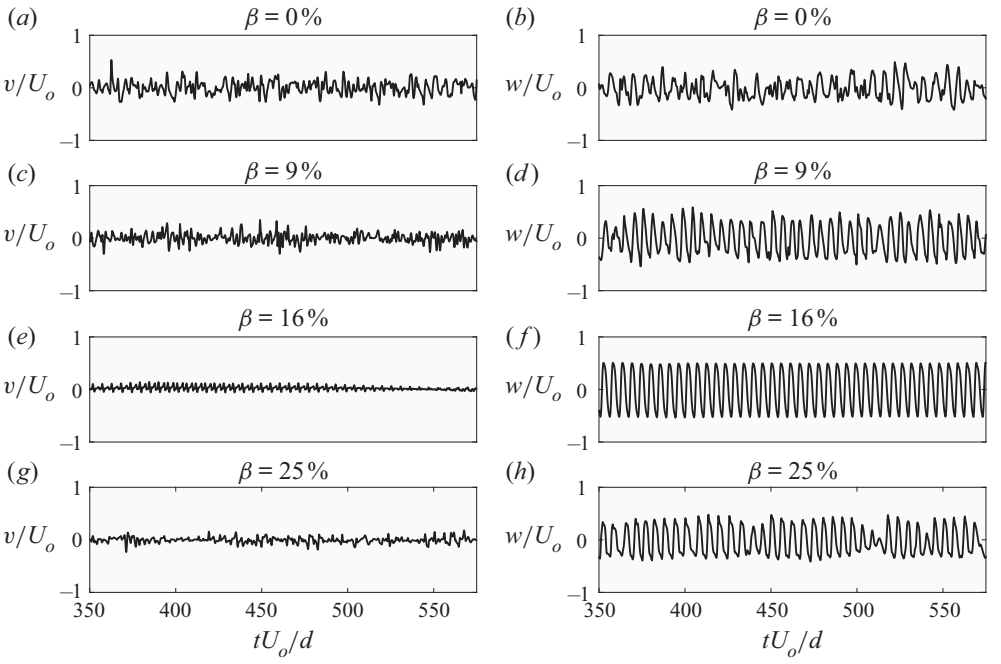

Figure 9. Velocity time trace sampled in the 'far' wake (15d downstream of the plate along the top edge of the plate, $y/d = 0$, $z/d = 8.5$): (a,c,e,g) v/U_o, (b,d,f,h) w/U_o.

3.5. *Two-point correlation*

Figure 11 shows the spanwise two-point correlation of all the velocity components in the 'near' and 'far' wakes. Here, the correlation coefficient is defined as $\rho_{\phi\phi} = \overline{\hat{\phi}(x, y, z, t)\,\hat{\phi}(x, y + \delta y, z, t)}/\overline{\hat{\phi}(x, y, z, t)^2}$, where $\hat{\phi} \in (\hat{u}, \hat{v}, \hat{w})$. The overline signifies time averaging over 75 vortex-shedding cycles. In the 'near' wake, the streamwise and cross-stream velocity components remain highly correlated at lower β (see ρ_{uu} and ρ_{ww}, respectively, in figures 11a,e) due to the formation of a spanwise-coherent Kármán vortex street (see figure 4). The correlation is lower at higher β as the dominant 'bleed' flow suppresses the vortex shedding. Here, the oscillatory nature of correlation for perforation cases, i.e. at $\beta > 0\,\%$, is due to the effect of periodically spaced 'bleed' flow through holes. For similar reasons, the uncorrelated nature of the spanwise velocity component at $\beta = 0\,\%$ deviates marginally with increasing β (see ρ_{vv} in figure 11c). The irregular behaviour of the correlation functions along the span could be due to the limited number of samples considered for averaging (Singh & Narasimhamurthy 2021). In the 'far' wake, the streamwise and cross-stream correlations remain correlated in all cases (see figures 11b,f) due to the presence of spanwise vortex tubes (see figure 4). Interestingly, ρ_{uu} and ρ_{ww} follow a trend similar to that of St_d, where the correlation increases with β at 0 % to 16 %, followed by a slight drop at 25 %. Also, ρ_{vv} shows a similar trend with negative correlation (see figure 11d). Thus it can be noted that all the velocity components show high correlation at $\beta = 16\,\%$ due to 'quasi-periodic' vortex tubes in the 'far' wake (see figure 4).

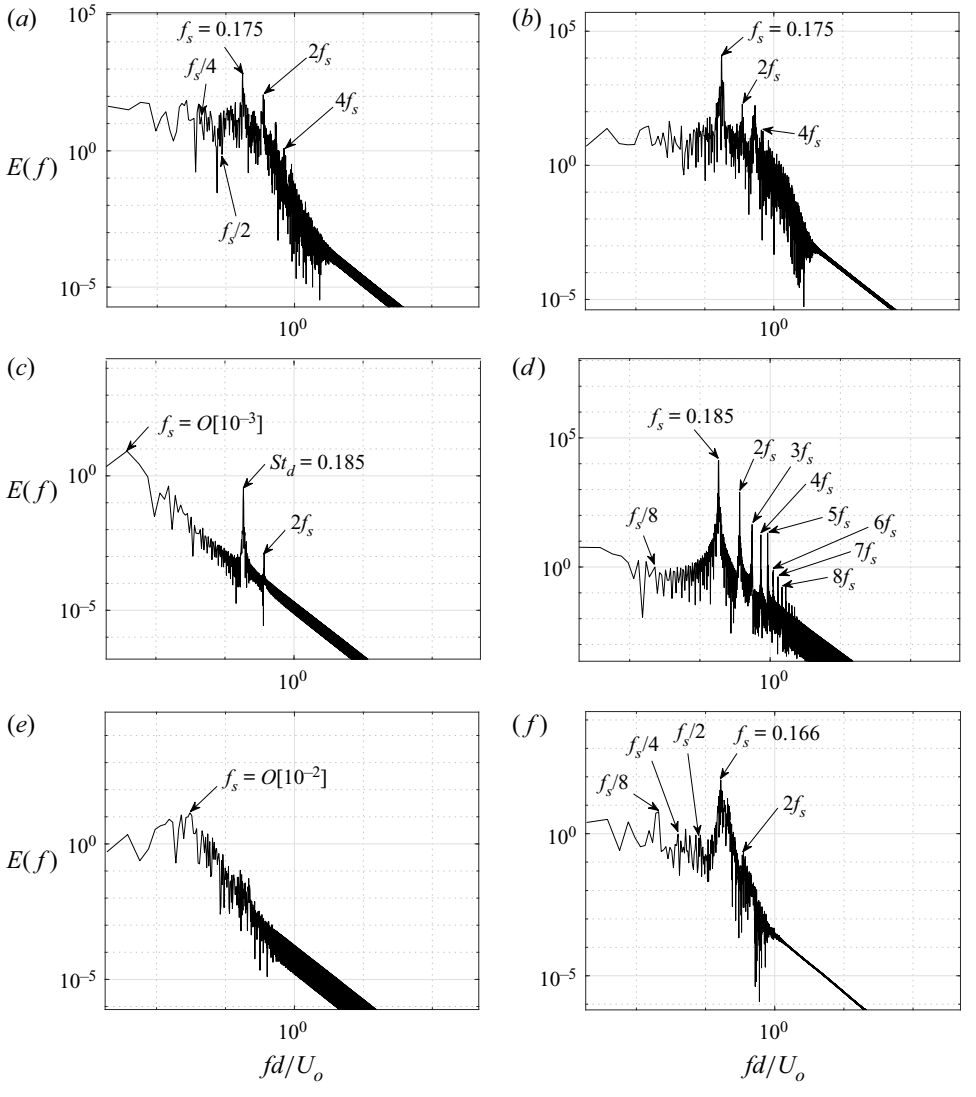

Figure 10. Fast Fourier transforms of the $\hat{w}$ velocity sampled at (*a*,*c*,*e*) the 'near' wake (1*d* downstream along the top edge of the plate, $y/d = 0$, $z/d = 8.5$), and (*b*,*d*,*f*) the 'far' wake (15*d* downstream along the top edge of the plate, $y/d = 0$, $z/d = 8.5$), for (*a*,*b*) $\beta = 9\,\%$, (*c*,*d*) $\beta = 16\,\%$, (*e*,*f*) $\beta = 25\,\%$. Here, f_s denotes the dominant St_d.

3.6. *Modes of instability*

Figure 12 shows the iso-contours of streamwise vorticity at all β considered in the present study. The instability mode for the non-perforated plate is reported to have mode B vortex structure by Najjar & Balachandar (1998), where reasonably well organized streamwise vortices with spanwise wavelength ≈ 1.2 are observed to extend in the braid region connecting the Kármán vortices. The strain field induced by the streamwise vorticity significantly distorts the spanwise Kármán vortices. Nevertheless, the spanwise and streamwise vortices are observed to be distinct (see figure 5). Although the vortex structure is observed to be slightly chaotic at lower porosities in the present study,

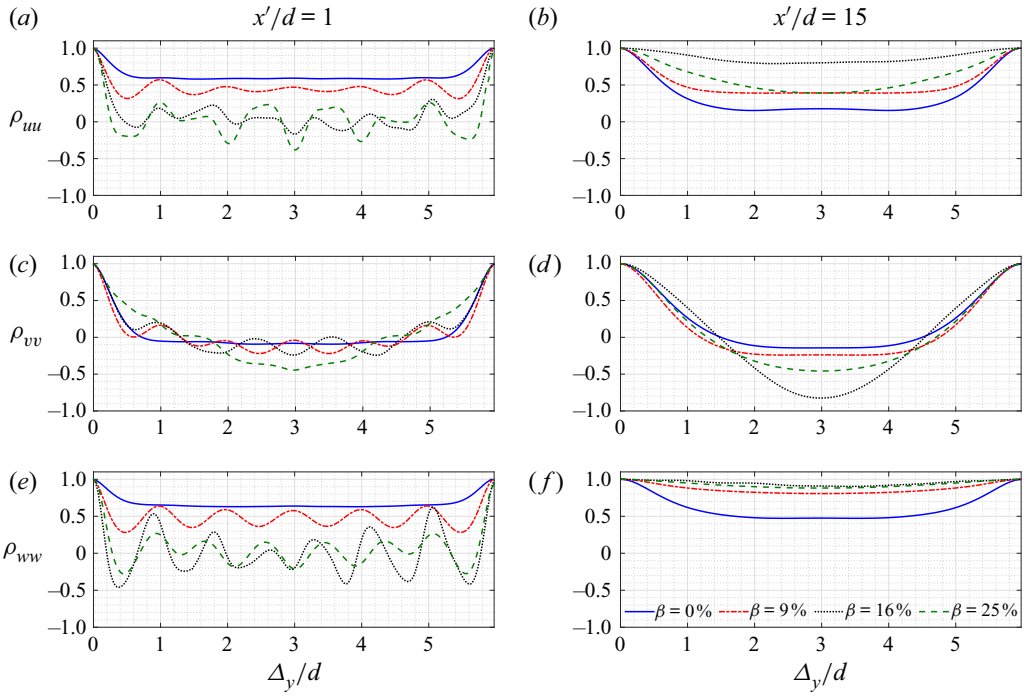

Figure 11. Two-point correlation ρ at (a,c,e) the 'near' wake ($1d$ downstream along the top edge of the plate, $z/d = 8.5$), and (b,d,f) the 'far' wake ($15d$ downstream along the top edge of the plate, $z/d = 8.5$), for (a,b) $\widehat{uu}$, (c,d) $\widehat{vv}$, (e,f) $\widehat{ww}$.

the symmetry pattern at the higher porosity of $\beta = 16\,\%$ appears similar to a mode B structure observed by Williamson (1996*b*) for circular cylinder wakes, where mode B is defined as a secondary vortex structure with symmetric pattern of streamwise vortices from one braid region to the next. Figure 12 further indicates the effect of perforation on the secondary instabilities. Here, the vortical structures with spanwise wavelength $\approx 1d$ in the 'near' wake of perforation cases correspond to the vorticity arising due to the effect of 'bleed' flow. In the 'far' wake, it appears that the prevailing secondary instability tends towards coherence and spatial compactness as β is increased up to 16 %. The spanwise wavelength of this transition mode in the present perforated case is $\approx 1d$ (i.e. six pairs along the span), in contrast to $\approx 2d$ of the short-wavelength mode reported for non-perforated plates (Julien *et al.* 2003, 2004; Thompson *et al.* 2006) and $\approx 1d$ of mode B reported for circular cylinders (Williamson 1996*a*). The spanwise coherence is also seen to increase for Kármán vortex structures. At $\beta = 16\,\%$, the wake instability (cf. figures 5*c* and 12*c*) appears to behave as quasi-laminar since the wake experiences periodic oscillations (cf. figure 9(*b*,*d*,*f*,*h*)). However, there exists the presence of fine-scale streamwise vortex structures. This case resembles closely the resonance state of the wake behind circular cylinders (Williamson 1996*b*). Further, figure 12(*d*) indicates that the prevailing secondary instability in the 'far' wake at $\beta = 25\,\%$ is signified by an antisymmetric pattern of streamwise vortices having spanwise wavelength $\approx 2d$. This flow state has some resemblance to the mode A instability in the wake of circular cylinders.

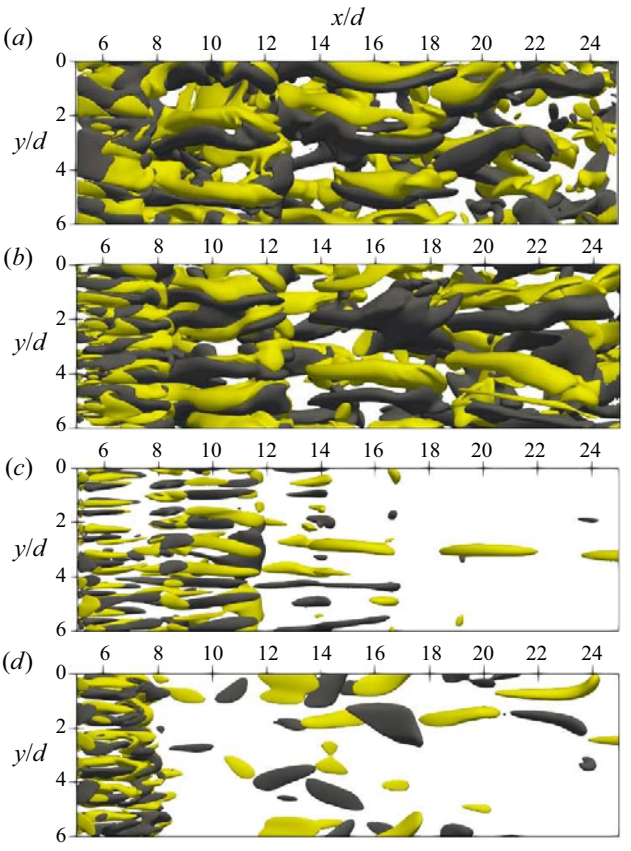

Figure 12. Three-dimensional iso-contours of streamwise vorticity $\omega_x = \pm(0.002\text{–}0.003)$, for (*a*) $\beta = 0\,\%$, (*b*) $\beta = 9\,\%$, (*c*) $\beta = 16\,\%$, (*d*) $\beta = 25\,\%$. Yellow and black colours indicate positive and negative values of ω_x, respectively.

3.7. *Bleed flow (jet) oscillation*

In this study, we also observed another interesting phenomenon, where the jet or 'bleed' flow is experiencing an oscillatory motion along the spanwise direction (i.e. in the x–y plane). This meandering jet instability is captured in the instantaneous rotation rate field, defined by $\Omega_z = \partial u/\partial y - \partial v/\partial x$ (cf. figure 13). It appears that the meandering instability is profound as β is increased to 25 %. It has been reported in the literature that if the pitch c/h or the gap is sufficiently small, then the adjacent shear layers in a wake can experience proximity interference effects leading to engulfment or meandering oscillations and instabilities (Dadmarzi *et al.* 2018). The time trace of spanwise and cross-stream velocities sampled in the 'near' wake at the jet-central location (cf. figure 14) further substantiates this instability. Here, it is observed that the 'bleed' flow at $\beta = 9\,\%$ experiences low-frequency oscillations in the spanwise direction. In addition, it undergoes high-frequency oscillations in the cross-stream direction, indicating a strong influence of the vortex street. At $\beta = 16\,\%$, the 'bleed' flow undergoes high-frequency oscillations in both the spanwise and cross-stream directions. The low amplitude of v and w velocity signals are in line with reduced three-dimensionality and vortex shedding suppression, respectively. At $\beta = 25\,\%$, high-frequency high-amplitude jet meandering is evident from

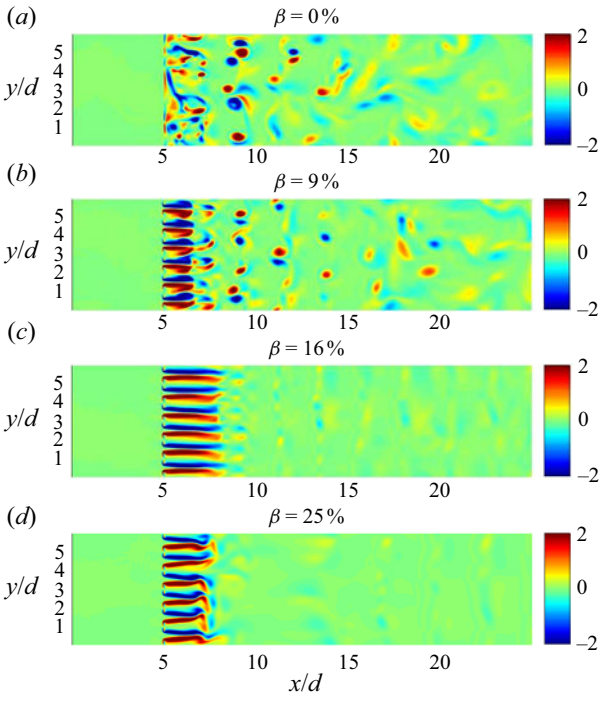

Figure 13. Instantaneous rotation rate at the wake centreline ($z/d = 8$) showing the flapping mechanism of the 'bleed' flow through the holes (jet).

the oscillatory high-frequency v velocity signal. At the same time, a low-amplitude w velocity signal signifies the absence of Kármán vortex shedding. The frequency of meandering is further quantified by the fast Fourier transform of the $\hat{v}$ velocity signal (cf. figure 15). The corresponding St_d at $\beta = 9\,\%$ is found to be negligibly small. On the other hand, the dominant meandering frequency is significantly higher at $\beta \geqslant 16\,\%$ with $St_d = 0.187$.

3.8. *Mean primary and secondary flow*

Figure 16 shows the mean streamwise velocity along the plate centreline, i.e. through the solid section of the plate, as well as along the hole centreline. The region along the x axis with negative velocity signifies the presence of a recirculation zone. From figure 16(a), it is observed that the primary recirculation zone, i.e. the recirculation along the plate centreline, is present predominantly at all β. However, the secondary recirculation, i.e. recirculation along the hole centreline shown in figure 16(b), diminishes in size and eventually disappears at $\beta = 25\,\%$. This is due to the fact that the 'bleed' flow pushes the vortex downstream with increasing β. Furthermore, the peak streamwise velocity with $\bar{u}/U_o > 1$ shows the jet-like effect of the 'bleed' flow. It appears that the peak jet velocity reduces while its location is shifted downstream with increase in β from 9 % to 25 % (also quantified earlier as $\bar{u}/U_{ojet,max}$ in table 4).

Additionally, a strong mean secondary flow (i.e. the spanwise velocity $\bar{v}/U_o$) is observed both upstream and downstream of the perforated plates. Figures 17(a,c) show contours of mean secondary flow upstream and downstream of the plate, respectively, at $\beta = 9\,\%$.

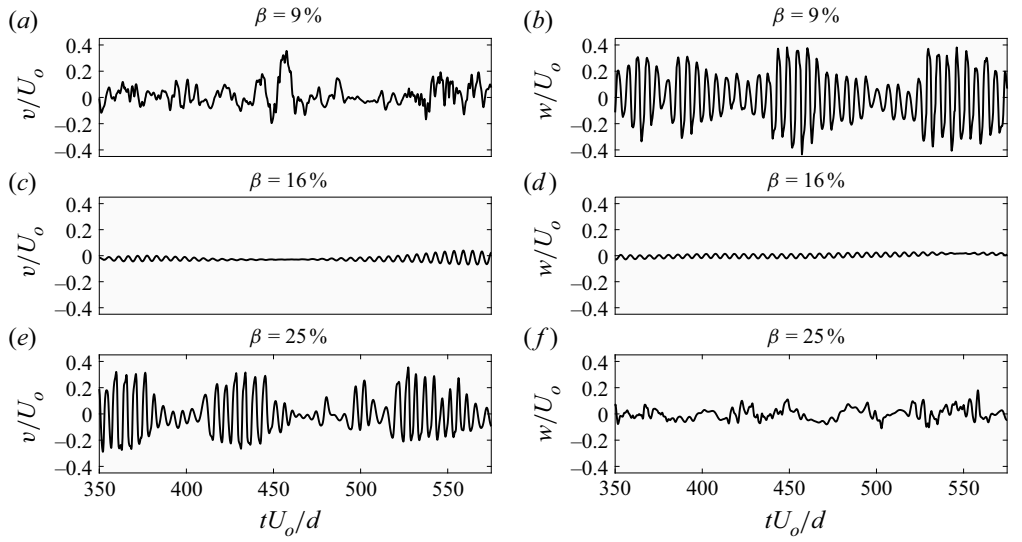

Figure 14. Velocity time trace sampled at $y/d = 2.5$, $z/d = 8$ (i.e. along the centreline of the third hole), for (a,c,e) v/U_o, (b,d,f) w/U_o. Sampling across the streamwise direction is done at $1d$ downstream of the plate for $\beta = 9\,\%$ or $2d$ downstream of the plate for $\beta \geqslant 16\,\%$ due to differential jet length.

The corresponding mean pressure contours are shown in figures 17(b,d). Note that the data are averaged in time and along the pitch. It appears that the maximum secondary flow upstream of the plate occurs at $y/d \approx 0.35$ and 0.65. This location corresponds to the edge of the square hole. The corresponding pressure contours show a high-pressure region away from the hole, indicating that the flow is driven by differential pressure towards the hole along the path of least resistance. In comparison, the maximum secondary flow downstream of the perforated plates is observed to be $\approx$15 % of the inflow velocity. Similar observations can be made at higher β (not shown here). Further, figure 18 shows the variation of mean secondary flow along the streamwise direction at various spanwise locations. It is clear from figure 18(b) that the mean secondary flow downstream of the perforated plates is significantly higher in the formation region. In contrast, the mean secondary flow is negligibly small for the non-perforated plate. In the 'far' wake, it reduces to a negligible value for both the perforated and non-perforated cases.

4. Conclusion

In the present DNS study, the effect of perforation on the wake of a low-Re turbulent flow over a flat plate placed normal to the free stream is studied. It is observed that the current mean drag coefficient $\overline{C_d}$, and the Strouhal number St_d, have excellent qualitative agreement with the high-Re experiments of Castro (1971), i.e. despite the differences in Re_d and perforation shape pattern. Further, the vortex street is pushed farther downstream by the bleed (jet) flow through the perforations, leading to monotonically decreasing $\overline{C_d}$ with respect to β. As β is increased, the spanwise vortex tubes in the near wake cease to exist, paving their way to streamwise vortex filaments signifying the bleed flow. Under its influence, the shear layers undergo undulations in the near wake, while their interaction is pushed farther downstream with the emergence of a vortex street in the far wake. The vortex street suppression leads to a sharp fall in $\overline{C_d}$, with its apparent reduction

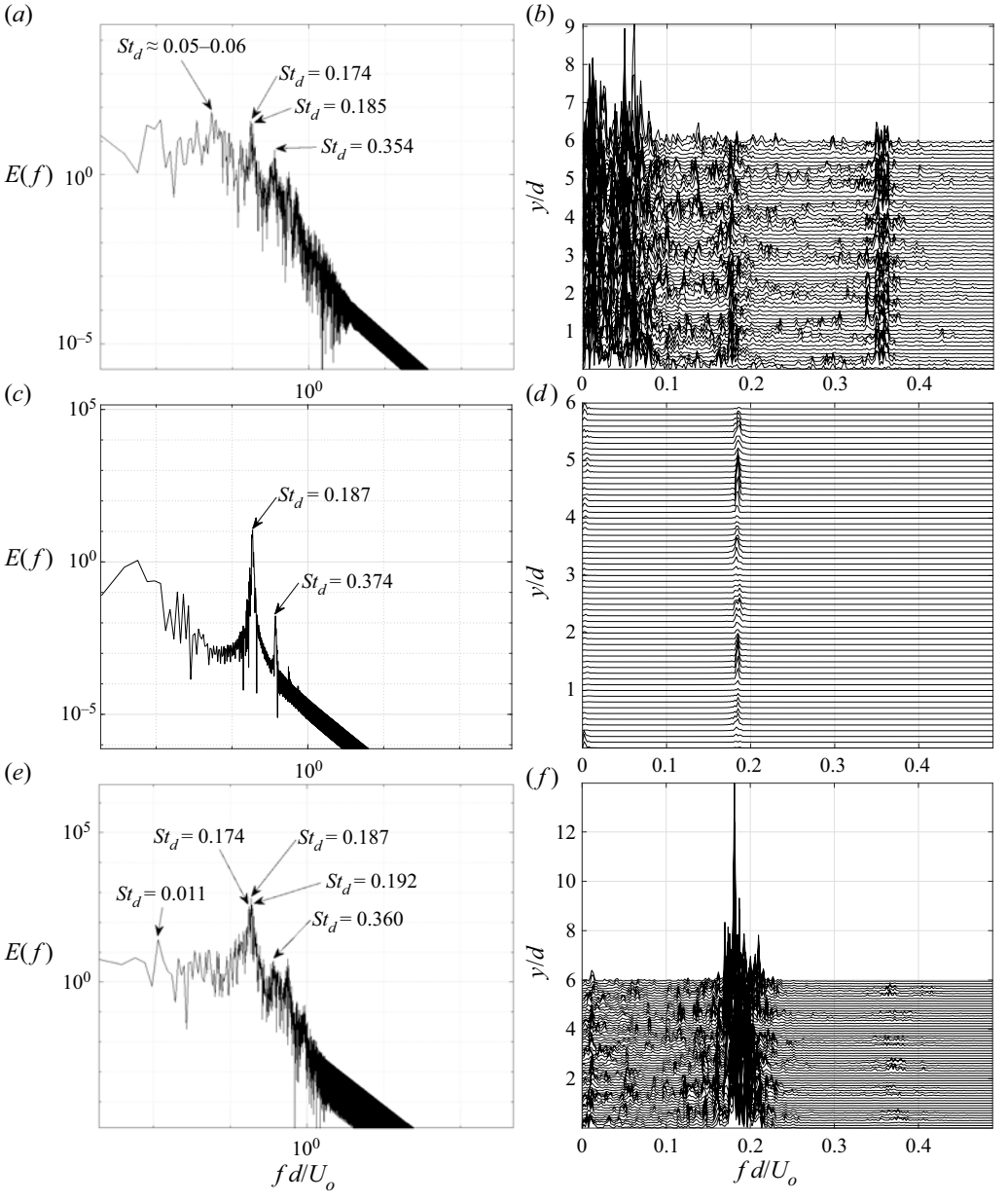

Figure 15. (*a*,*c*,*e*) Fast Fourier transforms of the $\hat{v}$ velocity sampled at $y/d = 2.5$, $z/d = 8$ (i.e. along the centreline of the third hole), and (*b*,*d*,*f*) spectra along the span, at (*a*,*b*) $\beta = 9\,\%$, (*c*,*d*) $\beta = 16\,\%$, (*e*,*f*) $\beta = 25\,\%$. Sampling along the streamwise direction is done at $1d$ downstream of the plate for $\beta = 9\,\%$ or $2d$ downstream of the plate for $\beta \geqslant 16\,\%$ due to differential jet length.

observed to begin at $\beta \approx 4\,\%$. Castro (1971) observed this phenomenon at $\beta \approx 20\,\%$. Such a dissimilarity may be a consequence of the vast difference in Re in both studies. In contrast, the increase in St_d with respect to β followed by a sudden drop at $\beta \approx 20\,\%$ is predicted in both studies. In the present study, a distinct dominant frequency exists at $\beta \geqslant 16\,\%$ in the near wake and far wake, corresponding to the shear layer undulations and

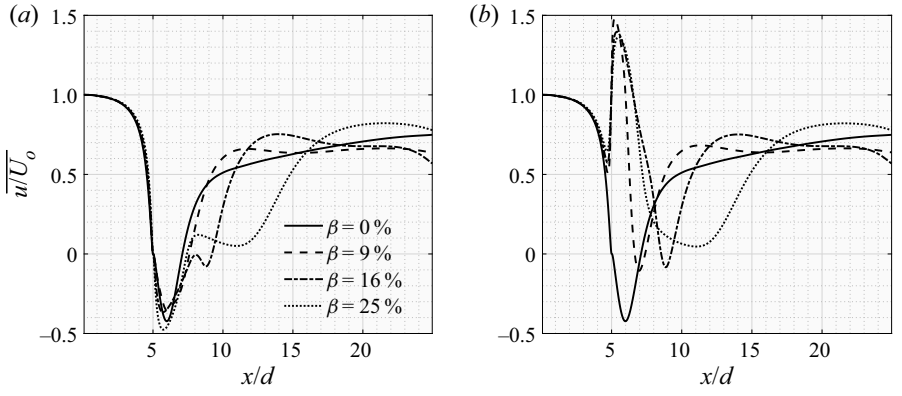

Figure 16. Mean primary flow along (*a*) the plate centreline, and (*b*) the hole centreline (averaged in time and along the pitch).

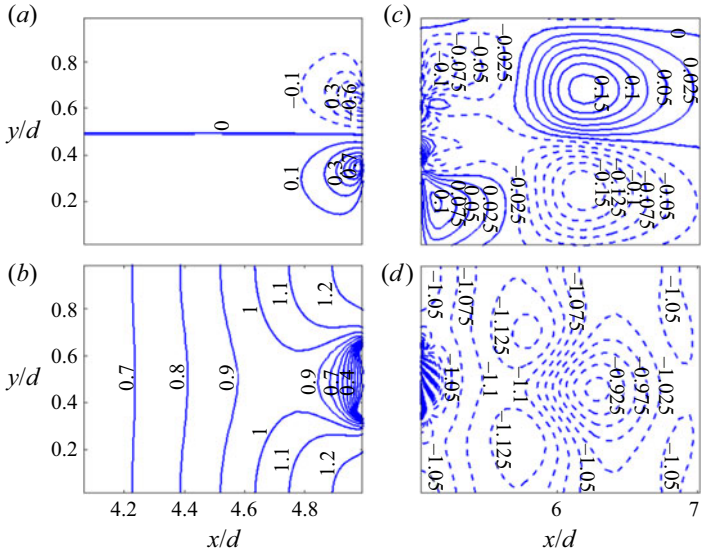

Figure 17. Secondary flow (averaged in time and along the pitch) at $z/d = 8$ (i.e. mid z plane) for $\beta = 9\,\%$: (*a*) $\bar{v}/U_o$ upstream of the plate; (*b*) $\bar{p}/(\rho U_o^2)$ upstream of the plate; (*c*) $\bar{v}/U_o$ downstream of the plate; (*d*) $\bar{p}/(\rho U_o^2)$ downstream of the plate.

the vortex street, respectively. This is in contrast to a single dominant frequency reported by Castro (1971), where the origin of the signal recording position is not particularly clear. Additionally, a higher magnitude of St_d is observed here when compared to that reported by Castro (1971). This can be attributed to the lower Re_d in the current DNS. Castro (1971) suggests two distinct flow regimes appropriate to low and high porosities, with a sudden transition between the two regimes at this point as a consequence of a vortex street suddenly ceasing to exist. Here, it was presumed that the bleed flow is just enough to prevent shear layer interaction completely. Also, the dominant frequency was believed to be due to some kind of far wake instability, where the two shear layers are assumed to coalesce downstream, leading to a flapping wake. On the other hand, Huang *et al.* (1995) and Huang & Keffer (1996) propose that the small-scale vortices in the formation region

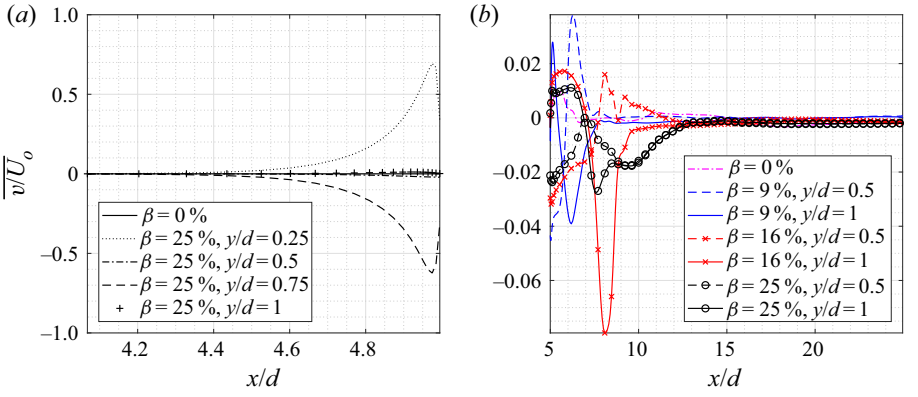

Figure 18. Secondary flow averaged in time and along the pitch, $\bar{v}/U_o$, at $z/d = 8$ (i.e. mid z plane): (a) upstream of the plate; and (b) downstream of the plate.

merge to form quasi-periodic Kármán-like structures in the far wake at high porosities. In contrast, the shear layers are observed to interact farther downstream to form a vortex street at least up to $\beta = 25\,\%$ in the present study. Note that such a dissimilarity may be a direct consequence of the *Re* effect and limited porosity cases considered here.

In the current study, a low-*Re* turbulent wake from a non-perforated plate is altered to a transitional state by the presence of perforation. The flow gradually relaminarizes , i.e. suppresses turbulence, as β is increased from 0 % to 16 %. The strong bleed flow at $\beta = 16\,\%$ renders the wake 'quasi-laminar' with weak flow three-dimensionality. This explains the increase in St_d when β is increased from 0 % to 16 %. Note that the near wake characterized by the jet or bleed flow also undergoes a similar reduction in flow three-dimensionality. At a higher β of 25 %, the spanwise vortex tubes undergo helical twisting and stretching with a drop in St_d. Such a behaviour is coupled with the revival of three-dimensionality in the near wake due to the proximity interference effects of adjacent jets. The enhanced proximity effects (when pitch separation is equivalent to the hole size) also cause the jets to be meandering at $St_d = 0.187$. Thus it is clear that the local Reynolds number Re_h (defined based on the hole size) in the near wake determines the overall three-dimensionality of the flow, and the near wake influences the behaviour of large vortical structures in the far wake. Nevertheless, it is quite possible that the wake and bleed flow vortex dynamics is different at much higher *Re*. In particular, the near wake may also be a function of the geometry (e.g. shape and size) of the perforations. It may be expected that a smaller hole size at a given β may increase flow retardation, while a larger hole size may increase bleed jet coalescence or meandering.

As a result of turbulence suppression, the streamwise vortex pairs of secondary instabilities become fairly regular and organized as β is increased from 0 % to 16 %. The 'quasi-laminar' state at $\beta = 16\,\%$ is coupled with the existence of fine-scale streamwise vortices structured in an orderly manner. The prevailing secondary instability at this porosity value appears similar to a mode B structure, with a symmetric pattern of streamwise vortices from one braid region to the next, with spanwise wavelength $\approx 1d$. However, at higher porosity $\beta = 25\,\%$, the secondary instability is signified by an antisymmetric pattern of streamwise vortices, with spanwise wavelength $\approx 2d$. Note that such an instability is observed to occur intermittently in space and time, resembling mode A instability reported by Williamson (1996*a*).

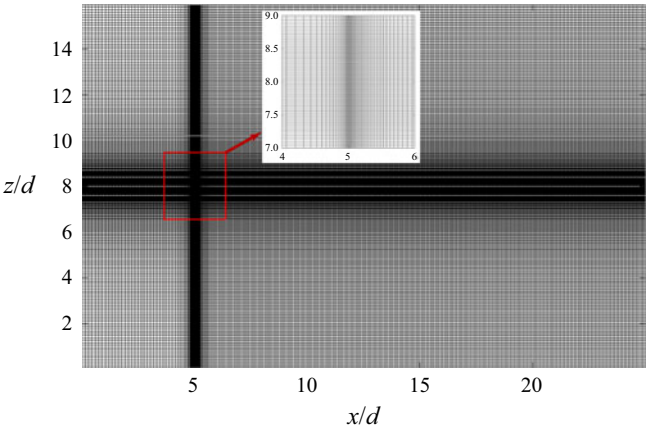

Figure 19. Mesh topology in an x–z plane.

Mesh	Case	N_x	N_y	N_z	St_d	$\overline{C_d}$
Two-dimensional	Normal flat plate ($h/d = 0$)	180	—	185	0.152	3.137
		320	—	260	0.152	3.289
		584	—	512	0.152	3.297
Two-dimensional	Side-by-side plates ($h/d = 0.5$)	180	—	185	0.172	2.180
		320	—	260	0.162	2.103
		584	—	512	0.163	2.198
Three-dimensional	Perforated plate, $\beta = 25\,\%$	320	60	260	0.213	1.492
		320	120	260	0.162	1.567
		320	240	260	0.166	1.577

Table 6. Mesh convergence test. The Strouhal number St_d is recorded at $15d$ downstream of the plate. Here, h refers to the hole or gap size between the plates. See Singh & Narasimhamurthy (2021) for more details.

Funding. This work has received support from the Centre for Industrial Consultancy and Sponsored Research, IIT Madras and the P.G. Senapathy Center for Computing Resource through a grant of computing time. The authors also thank P. Jadhav and D.I. Poojary, Department of Applied Mechanics, Indian Institute of Technology Madras, for facilitating additional DNS jobs on the cluster.

Declaration of interests. The authors report no conflict of interest.

Author ORCIDs.
Vagesh D. Narasimhamurthy https://orcid.org/0000-0002-1759-3186.

Appendix A. Grid verification

Two-dimensional simulations of flow over a normal flat plate and two side-by-side plates are considered first as limiting cases of the present perforated plate. The resulting mesh $[N_x, N_z]$ from the grid test (see figure 19) is then used for the 3-D grid study (perforated plate of $\beta = 25\,\%$), where equidistant grid size (Δ_y) is varied along the span. Table 6 summarizes the results. Here, the Strouhal number and mean drag coefficient, defined as $St_d = fd/U_o$ and $\overline{C_d} = (\bar{p}_{front} - \bar{p}_{back})/(0.5\rho U_o^2)$, respectively, are used as the criteria for a grid independence study, where f is the dominant wake frequency, and ρ is the fluid density. Here, $\bar{p}_{front}$ and $\bar{p}_{back}$ denote the mean pressures on the front and back surfaces of the plate, respectively.

AR	St_d	$\overline{C_d}$
1	0.168	1.585
3	0.168	1.582
6	0.166	1.577
12	0.164	1.573

Table 7. The Strouhal number St_d and mean drag coefficient $\overline{C_d}$ for various aspect ratios AR of a perforated plate at $\beta = 25\,\%$. Here, St_d is recorded in the far wake at $15d$ downstream along the top edge of the plate, $z/d = 8.5$.

Appendix B. Spanwise domain verification

The effect of spanwise extent of the domain on the Strouhal number, drag coefficient and wake dynamics is assessed by varying the spanwise length of the plate. Here, the aspect ratio AR, defined as the ratio of domain span to width of the plate, is varied between 1, 3, 6 and 12. It is observed from table 7 that the integral quantities St_d and $\overline{C_d}$ do not vary much with AR. This could be explained by the vortex street formation region, where the primary recirculation zone is pushed downstream by the bleed flow, irrespective of AR. On the other hand, the wake dynamics is starkly different at $AR \leqslant 3$ and $AR \geqslant 6$, as shown by the instantaneous vortex topology of λ_2 contours in figure 20. The wake at $AR \leqslant 3$ is fairly coherent with spanwise vortex cores parallel to the plate span. At $AR \geqslant 6$, the wake experiences incoherence of the spanwise vortex cores (see Singh & Narasimhamurthy (2021) for more details). From a computational cost perspective, $AR = 6$ is therefore chosen for further studies.

Appendix C. Influence of domain blockage

The blockage effect has been examined for a perforated plate of porosity $\beta = 25\,\%$. Here, two domains of blockage ratios 6.25 % and 3.125 % are considered (see table 8 for details). The blockage B is defined by d/L_z. The mesh size in the large domain, $[N_x, N_y, N_z] = [360, 240, 420]$, is such that the grid quality remains the same. It is observed that the drag coefficient varies by about 7.2 % between the cases. Such a variation is expected in bluff-body flows in (finite domain) numerical studies and closed wind tunnel experiments (also seen in the experiments of Fage & Johansen (1927) and reported by Maskell (1965)). Maskell (1965) proposed the following equation for blockage correction, where $\overline{C_{dc}}$ is the corrected drag coefficient, and ϵ is the blockage constant equal to 0.96:

$$\frac{\overline{C_d}}{\overline{C_{dc}}} = 1 + \epsilon \overline{C_d} B. \tag{C1}$$

It can also be noted from table 8 that the corrected drag coefficient from the present domain is close to the computed drag coefficient from the larger domain. Furthermore, the 3-D λ_2 contours are depicted in figure 21 for domains with blockage ratios 6.25 % and 3.125 %, respectively. (The plate is located at $x/d = 5$ for the present domain, and $x/d = 11$ for the larger domain.) Here, similarities are observed in both cases, such as the near wake structures, emergence of spanwise structures at $\approx 5d$ downstream of the plate, emergence of a vortex street at $\approx 12d$ downstream of the body, and existence of streamwise structures originating from the vortex tube located close to the outlet. The streamwise vorticity

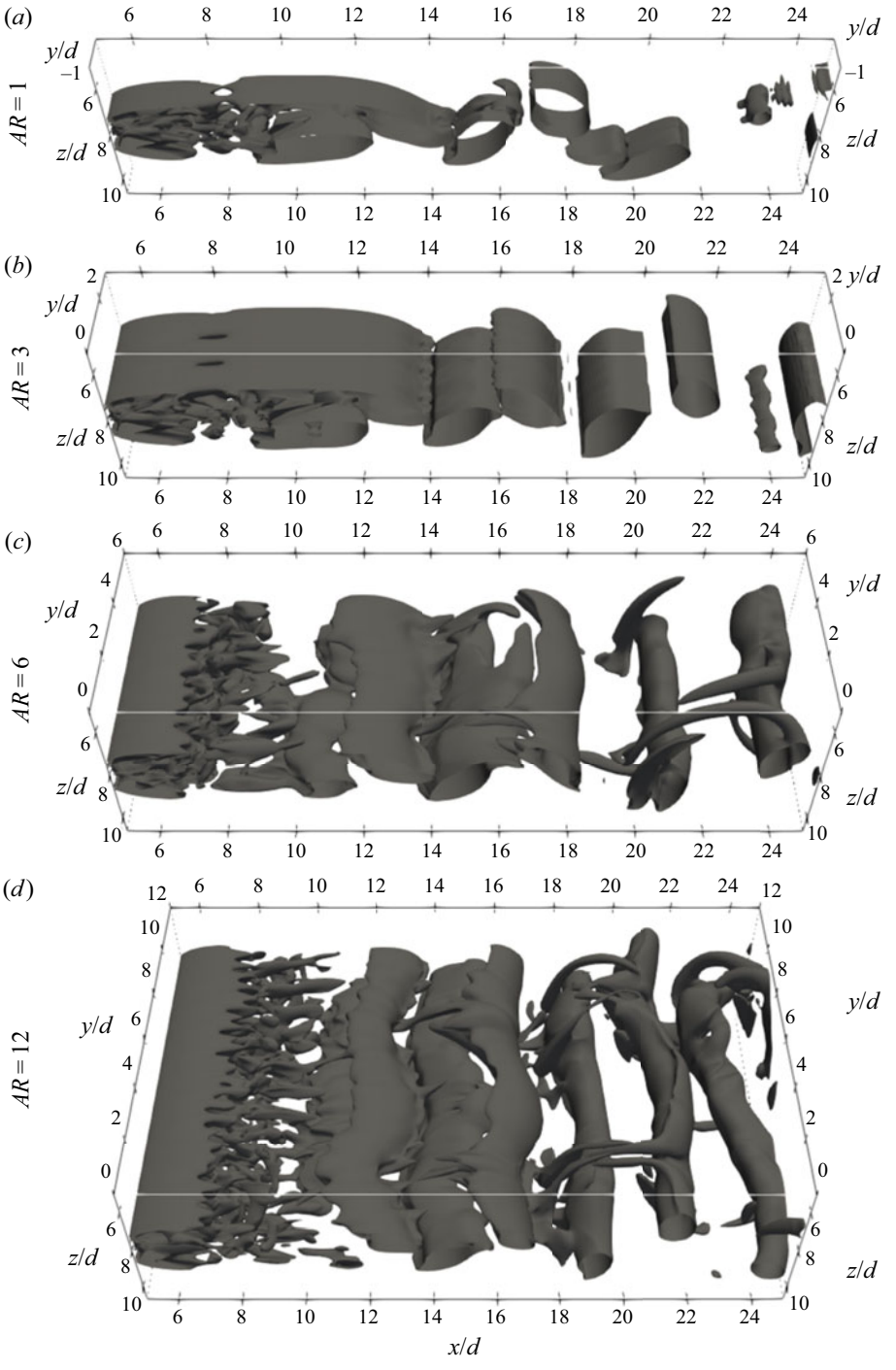

Figure 20. Instantaneous λ_2 contours depicting vortex topology for various AR of perforated plate at $\beta = 25\,\%$.

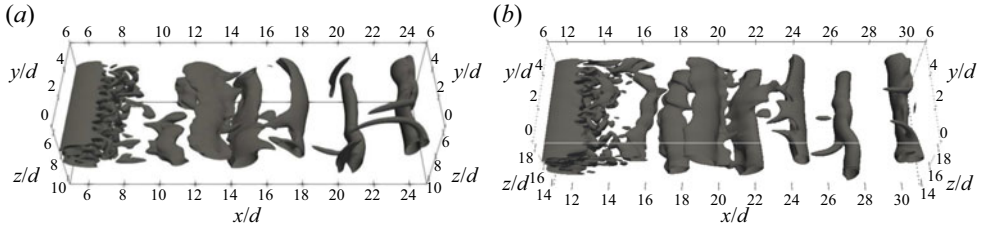

Figure 21. Instantaneous λ_2 from -3×10^{-6} to -4×10^{-6} depicting the vortex topology of a perforated plate at $\beta = 25\,\%$: (*a*) domain $L_x \times L_y \times L_z = 25 \times 6 \times 16$; (*b*) domain $L_x \times L_y \times L_z = 31 \times 6 \times 32$.

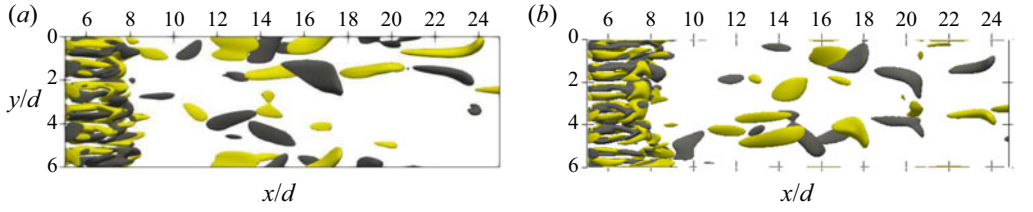

Figure 22. Instantaneous 3-D iso-contours of streamwise vorticity $\omega_x = \pm(0.002\text{–}0.003)$ of a perforated plate at $\beta = 25\,\%$. Yellow and black colours indicate positive and negative values of ω_x, respectively: (*a*) domain $L_x \times L_y \times L_z = 25 \times 6 \times 16$; (*b*) domain $L_x \times L_y \times L_z = 31 \times 6 \times 32$.

Case	L_{xu}	L_z	L_y	Blockage ratio	$\overline{C_d}$	$\overline{C_{dc}}$	St_d
Present	$5d$	$16d$	$6d$	6.25 %	1.577	1.440	0.166
Large	$11d$	$32d$	$6d$	3.125 %	1.463	1.401	0.153

Table 8. Influence of domain blockage on $\overline{C_d}$ and St_d for a perforated plate at $\beta = 25\,\%$. Here, the domain length is varied in the streamwise (upstream of the plate) and cross-stream directions. The blockage ratio is defined as $(d/L_z) \times 100$.

contours shown in figure 22 depict similar behaviour in both the cases. Considering the computational cost, the present domain is chosen for further parametric studies.

References

Afgan, I., Benhamadouche, S., Han, X., Sagaut, P. & Laurence, D. 2013 Flow over a flat plate with uniform inlet and incident coherent gusts. *J. Fluid Mech.* **720**, 457–485.

Alfonsi, G., Primavera, L. & Felisari, R. 2003 On the behavior of POD modes of the flow past a perforated plate. *J. Flow Vis. Image Process.* **10** (1–2), 105–117.

Antonia, R.A., Zhou, T. & Romano, G.P. 2002 Small-scale turbulence characteristics of two-dimensional bluff body wakes. *J. Fluid Mech.* **459**, 67–92.

Bae, Y. & Kim, Y.I. 2016 Numerical modeling of anisotropic drag for a perforated plate with cylindrical holes. *Chem. Engng Sci.* **149** (Supplement C), 78–87.

Bevilaqua, P.M. & Lykoudis, P.S. 1978 Turbulence memory in self-preserving wakes. *J. Fluid Mech.* **89** (3), 589–606.

Cannon, S., Champagne, F. & Glezer, A. 1993 Observations of large-scale structures in wakes behind axisymmetric bodies. *Exp. Fluids* **14** (6), 447–450.

Castro, I.P. 1971 Wake characteristics of two-dimensional perforated plates normal to an air-stream. *J. Fluid Mech.* **46** (3), 599–609.

CHOI, C.-B. & YANG, K.-S. 2014 Three-dimensional instability in flow past a rectangular cylinder ranging from a normal flat plate to a square cylinder. *Phys. Fluids* **26** (6), 061702.

CIMBALA, J.M., NAGIB, H.M. & ROSHKO, A. 1988 Large structure in the far wakes of two-dimensional bluff bodies. *J. Fluid Mech.* **190**, 265–298.

DADMARZI, F.H., NARASIMHAMURTHY, V.D., ANDERSSON, H.I. & PETTERSEN, B. 2018 Turbulent wake behind side-by-side flat plates: computational study of interference effects. *J. Fluid Mech.* **855**, 1040–1073.

FAGE, A. & JOHANSEN, F.C. 1927 On the flow of air behind an inclined flat plate of infinite span. *Brit. Aero. Res. Coun. Rep. Memo* **1104**, 81–106.

GRAHAM, J.M.R. 1976 Turbulent flow past a porous plate. *J. Fluid Mech.* **73** (3), 565–591.

HEMMATI, A., WOOD, D.H. & MARTINUZZI, R.J. 2016 Characteristics of distinct flow regimes in the wake of an infinite span normal thin flat plate. *Intl J. Heat Fluid Flow* **62** (Part B), 423–436.

HIGUCHI, H., ZHANG, J., FURUYA, S. & MUZAS, B.K 1998 Immediate and near wake flow patterns behind slotted disks. *AIAA J.* **36** (9), 1626–1634.

HUANG, Z., FERRÉ, J.A., KAWALL, J.G. & KEFFER, J.F. 1995 The connection between near and far regions of the turbulent porous body wake. *Exp. Therm. Fluid Sci.* **11** (2), 143–154.

HUANG, Z., KAWALL, J.G. & KEFFER, J.F. 1996 Development of structure within the turbulent wake of a porous body. Part 2. Evolution of the three-dimensional features. *J. Fluid Mech.* **329**, 117–136.

HUANG, Z. & KEFFER, J.F. 1996 Development of structure within the turbulent wake of a porous body. Part 1. The initial formation region. *J. Fluid Mech.* **329**, 103–115.

INOUE, O. 1985 A new approach to flow problems past a porous plate. *AIAA J.* **23** (12), 1916–1921.

JEONG, J. & HUSSAIN, F. 1995 On the identification of a vortex. *J. Fluid Mech.* **285**, 69–94.

JULIEN, S., LASHERAS, J. & CHOMAZ, J.-M. 2003 Three-dimensional instability and vorticity patterns in the wake of a flat plate. *J. Fluid Mech.* **479**, 155–189.

JULIEN, S., ORTIZ, S. & CHOMAZ, J.-M. 2004 Secondary instability mechanisms in the wake of a flat plate. *Eur. J. Mech. (*B*/Fluids)* **23** (1), 157–165.

KANG, S.-H., LEE, H.-S., JEON, W.-P. & LEE, C.-H. 1989 Viscous flows through screens normal to the uniform stream. *KSME J.* **3** (2), 146–152.

KARNIADAKIS, G.E. & TRIANTAFYLLOU, G.S. 1992 Three-dimensional dynamics and transition to turbulence in the wake of bluff objects. *J. Fluid Mech.* **238**, 1–30.

KIM, H.-B. & LEE, S.-J. 2001 Hole diameter effect on flow characteristics of wake behind porous fences having the same porosity. *Fluid Dyn. Res.* **28** (6), 449–464.

KIM, H.-B. & LEE, S.-J. 2002 The structure of turbulent shear flow around a two-dimensional porous fence having a bottom gap. *J. Fluids Struct.* **16** (3), 317–329.

KOPP, G.A. & KEFFER, J.F. 1996 The near wake region of a high solidity mesh strip. *Phys. Fluids* **8** (10), 2712–2715.

LIU, M., XIE, C., YAO, M. & YANG, J. 2017 Study on the near wake of a honeycomb disk. *Exp. Therm. Fluid Sci.* **81** (Supplement C), 33–42.

LIU, R., TING, D.S-K. & RANKIN, G.W. 2004 On the generation of turbulence with a perforated plate. *Exp. Therm. Fluid Sci.* **28** (4), 307–316.

MANHART, M. 2004 A zonal grid algorithm for DNS of turbulent boundary layers. *Comput. Fluids* **33** (3), 435–461.

MASKELL, E.C. 1965 A theory of the blockage effects on bluff bodies and stalled wings in a closed wind tunnel. *Aeronautical Research Council* ARC-R/M-3400.

NAJJAR, F.M. & BALACHANDAR, S. 1998 Low-frequency unsteadiness in the wake of a normal flat plate. *J. Fluid Mech.* **370**, 101–147.

NAJJAR, F.M. & VANKA, S.P. 1995 Effects of intrinsic three-dimensionality on the drag characteristics of a normal flat plate. *Phys. Fluids* **7** (10), 2516–2518.

NARASIMHAMURTHY, V.D. & ANDERSSON, H.I. 2009 Numerical simulation of the turbulent wake behind a normal flat plate. *Intl J. Heat Fluid Flow* **30** (6), 1037–1043.

NARASIMHAMURTHY, V.D., ANDERSSON, H.I. & PETTERSEN, B. 2008 Cellular vortex shedding in the wake of a tapered plate. *J. Fluid Mech.* **617**, 355–379.

PELLER, N., LE DUC, A., TREMBLAY, F. & MANHART, M. 2006 High-order stable interpolations for immersed boundary methods. *Intl J. Numer. Meth. Fluids* **52** (11), 1175–1193.

PERERA, M.D.A.E.S. 1981 Shelter behind two-dimensional solid and porous fences. *J. Wind Engng Ind. Aerodyn.* **8** (1), 93–104.

RICHTER, D., IACCARINO, G. & SHAQFEH, E.S.G. 2010 Simulations of three-dimensional viscoelastic flows past a circular cylinder at moderate Reynolds numbers. *J. Fluid Mech.* **651**, 415–442.

RICHTER, D., IACCARINO, G. & SHAQFEH, E.S.G. 2012 Effects of viscoelasticity in the high Reynolds number cylinder wake. *J. Fluid Mech.* **693**, 297–318.

SHA, W.T. & LAUNDER, B.E. 1979 A model for turbulent momentum and heat transport in large rod bundles. *Tech. Rep.* ANL-77-73. Argonne National Laboratory.

SINGH, A. & NARASIMHAMURTHY, V.D. 2018 Perforated bluff-body wake simulations: influence of aspect ratio. In *IEEE 25th International Conference on High Performance Computing Workshops (HiPCW)*, pp. 32–35. IEEE Computer Society.

SINGH, A. & NARASIMHAMURTHY, V.D. 2021 Influence of aspect ratio on the wake of a perforated plate. *Prog. Comput. Fluid Dyn.* **21**, 355–368.

STEIROS, K. & HULTMARK, M. 2018 Drag on flat plates of arbitrary porosity. *J. Fluid Mech.* **853**, R3.

TAYLOR, G.I. 1944 Air resistance of a flat plate of very porous material. *Tech. Rep.* 2236. Aeronaut. Res. Counc. Rep. Memoranda.

THOMPSON, M.C., HOURIGAN, K., RYAN, K. & SHEARD, G.J. 2006 Wake transition of two-dimensional cylinders and axisymmetric bluff bodies. *J. Fluids Struct.* **22** (6), 793–806.

TIAN, X., ONG, M.C., YANG, J. & MYRHAUG, D. 2014 Large-eddy simulation of the flow normal to a flat plate including corner effects at a high Reynolds number. *J. Fluids Struct.* **49**, 149–169.

VILLERMAUX, E. & HOPFINGER, E.J. 1994 Periodically arranged co-flowing jets. *J. Fluid Mech.* **263**, 63–92.

WILLIAMSON, C.H.K. 1988 The existence of two stages in the transition to three-dimensionality of a cylinder wake. *Phys. Fluids* **31** (11), 3165–3168.

WILLIAMSON, C.H.K. 1996*a* Vortex dynamics in the cylinder wake. *Annu. Rev. Fluid Mech.* **28** (1), 477–539.

WILLIAMSON, C.H.K. 1996*b* Three-dimensional wake transition. *J. Fluid Mech.* **328**, 345–407.

WYGNANSKI, I., CHAMPAGNE, F. & MARASLI, B. 1986 On the large-scale structures in two-dimensional, small-deficit, turbulent wakes. *J. Fluid Mech.* **168**, 31–71.

XIAO, H., DUAN, L., SUI, R. & ROSGEN, T. 2013 Experimental investigations of turbulent wake behind porous disks. In *1st Marine Energy Technology Symposium*, pp. 1–11.